

Dynamic slab segmentation due to brittle–ductile damage in the outer rise

<https://doi.org/10.1038/s41586-021-03937-x>

T. V. Gerya¹✉, D. Bercovici² & T. W. Becker^{3,4,5}

Received: 30 September 2020

Accepted: 20 August 2021

Published online: 10 November 2021

 Check for updates

Subduction is the major plate driving force, and the strength of the subducting plate controls many aspects of the thermochemical evolution of Earth. Each subducting plate experiences intense normal faulting^{1–9} during bending that accommodates the transition from horizontal to downwards motion at the outer rise at trenches. Here we investigate the consequences of this bending-induced plate damage using numerical subduction models in which both brittle and ductile deformation, including grain damage, are tracked and coupled self-consistently. Pervasive slab weakening and pronounced segmentation can occur at the outer-rise region owing to the strong feedback between brittle and ductile damage localization. This slab-damage phenomenon explains the subduction dichotomy of strong plates and weak slabs¹⁰, the development of large-offset normal faults^{6,7} near trenches, the occurrence of segmented seismic velocity anomalies¹¹ and distinct interfaces imaged within subducted slabs^{12,13}, and the appearance of deep, localized intraplate areas of reduced effective viscosity¹⁴ observed at trenches. Furthermore, brittle–viscously damaged slabs show a tendency for detachment at elevated mantle temperatures. Given Earth's planetary cooling history¹⁵, this implies that intermittent subduction with frequent slab break-off episodes¹⁶ may have been characteristic for Earth until more recent times than previously suggested¹⁷.

The subduction of negatively buoyant oceanic lithosphere is a key driver of terrestrial tectonics. Subduction results from buoyancy forces that bend and pull the lithosphere into the interior of the Earth's mantle where mechanical properties of subducted lithospheric slabs are strongly modified by various physical–chemical processes^{10,18,19}. One of the large-scale effects of this modification is the pronounced mechanical dichotomy of stronger lithospheric plates at the surface and weaker slabs in Earth's interior, which has been proposed on the basis of various geological–geophysical observations combined with some analytical and numerical modelling^{10,19–23}. Whereas strong plates at the surface are a prerequisite for terrestrial-style, one-sided subduction^{10,24}, weakened lithospheric subducted slabs, which bend, stretch, pile, segment or lie flat at the top of the lower mantle, are needed to reproduce the spectrum of slab morphologies^{25,26}, observed bending curvatures²³, lateral changes in Earth's geoid^{18,27} and variations of intraslab seismicity with depth²². Slab weakening is in apparent contradiction with experimentally calibrated, thermally activated rheological laws for the lithospheric mantle²⁸, which predict high effective viscosity ($>10^{24}$ Pa s) of subducted slabs in the upper mantle¹⁸, implying a slab/mantle viscosity contrast of $\gg 1,000$. By contrast, a number of natural observables suggest that this contrast should be much lower (around 100–500)^{20,22,23,25,29}, for example, to reconcile the dynamics with seismic tomography models and slab seismicity distribution with depth that indicate strong bending, stretching and even disruption of subducted slabs in the upper mantle^{22,23,25,26,30}.

The apparent rheological paradox of strong plates and weak slabs^{10,18,25} can be resolved by assuming some additional lithospheric weakening processes that are intrinsically related to the transition from horizontal plate motion to its subduction into the mantle. In this respect, plate bending at the outer rise is a primary candidate for changing the mechanical properties of the lithosphere^{4,19}. Each subducting plate, irrespective of its age and earlier history, unavoidably experiences a transition from its horizontal to vertical motion through bending when passing through the outer-rise region that is present at every subduction trench. Plate bending is not fully elastic and is associated with a number of irreversible physical–chemical processes that can markedly weaken the mechanical properties of the subducting plate^{1,4,6–8,19}.

It is well understood that the colder, brittle top region of subducting plates is pervasively damaged by extensional outer-rise normal faulting^{1,4,7,9,19}, possibly associated with downwards water penetration and mantle lithosphere serpentinization^{2–5,8}. By contrast, the deeper and warmer portions of the plate deform in compression by both viscous creep¹⁴ and compressional faulting³¹. This deformation style indicates the existence of a barrier to the penetration of water and deeper chemical alteration of the plate. As the result, the deeper portion of the plate can be predominantly weakened by ductile damage processes such as grain-size reduction assisted by Zener pinning^{32–36}. Relating these brittle and ductile damage processes to the plate bending at the outer rise can advance our understanding of whether and how the pervasive weakening of subducting plates may occur in nature and what

¹Department of Earth Sciences, Swiss Federal Institute of Technology Zurich, Zurich, Switzerland. ²Department of Earth and Planetary Sciences, Yale University, New Haven, CT, USA. ³Institute for Geophysics, Jackson School of Geosciences, The University of Texas at Austin, Austin, TX, USA. ⁴Department of Geological Sciences, Jackson School of Geosciences, The University of Texas at Austin, Austin, TX, USA. ⁵Oden Institute for Computational Engineering & Sciences, The University of Texas at Austin, Austin, TX, USA. ✉e-mail: tgerya@ethz.ch

consequences that deformation memory will have for the dynamics and stability of subduction.

Here we investigate the consequences of bending-induced plate damage by using two-dimensional numerical thermomechanical subduction models in which both brittle–plastic and ductile deformation as well as grain-size evolution are coupled self-consistently (Methods). Our results indicate that brittle–ductile slab weakening and plate segmentation should occur at the outer-rise region owing to the strong feedback between brittle and ductile damage localization, and that this process can explain a range of observations from well imaged subduction zones.

Slab segmentation at the outer rise

Figure 1 shows an example of a typical model evolution resulting in subsiding slab damage and segmentation. The numerical experiment starts from subduction initiation at a transform fault^{24,37}, which separates two oceanic plates of different ages, leading to gravitational instability. The older plate starts to subduct in a retreating manner whereas the younger, now overriding, plate is subjected to extension and horizontal motion towards the retreating trench. After the initial period of retreat associated with gradual steepening of the slab, the slab angle stabilizes and the advancing horizontal motion of the subducting plate begins. This mode of subduction continues until the slab reaches the mantle transition zone and starts to flatten due to the negative Clapeyron slope of the spinel–perovskite phase transition (Methods), which initiates a new episode of trench retreat. The viscosity of the subducting plate that results from this dynamically self-consistent subduction scenario shows a pattern of 150–200-km-wide segments separated by narrow low-viscosity zones. This damage pattern forms as the result of linked, localized brittle–plastic deformation and grain-size reduction at the outer rise (Fig. 2a). As a consequence, the subducting slab deforms easily in a chain-like fashion in response to its interaction with the mantle transition zone. The resulting slab morphologies are markedly different from those of viscoplastic slabs without damage^{21,25} and reflect the influence of the strong coupling between the brittle and ductile strain-localization mechanisms during plate bending.

Model sensitivity studies show that the style of slab deformation depends strongly on both the ductile damage and the strain-induced weakening of faults as well as on the age of the subducting plate and the mantle potential temperature. In particular, deactivation of ductile damage (grain-size reduction) and/or strain-induced weakening produces smoothly bent slabs (compare Extended Data Fig. 2a, e and Extended Data Figs. 2b, f, 2c, g, 2d, h) comparable to previous subduction models^{16,21,24,25}. A lack of ductile damage also makes subduction initiation more difficult (compare Extended Data Fig. 3a, e and Extended Data Fig. 3c, g) owing to the increased bending resistance of the subducting plate, which should become older and denser to allow for spontaneous subduction initiation (compare Extended Data Fig. 3a, e and Extended Data Fig. 4c, g). The combined effects of fault weakening and ductile damage on slab segmentation are notably distinct from the individual forms of weakening. In the absence of normal fault weakening, slab segments are less pronounced and grain-size reduction inside the subducting plate is distributed more evenly owing to the weaker feedback between faulting and grain-size reduction (compare Extended Data Fig. 2a, e and Extended Data Figs. 2c, g, 4c, g, 4d, h). This, in turn, causes more distributed rather than strongly localized, segmented weakening of slabs. A similar effect is achieved by decreasing the rate of fault-weakening with strain (compare Extended Data Fig. 3b, f and Extended Data Fig. 3c, g). In the absence of ductile damage, slab segments remain but the displacement along individual normal faults is reduced (Extended Data Fig. 2b, f). As a result, the number of segments increases together with a decrease in the characteristic segment width (compare Extended Data Fig. 2a, e and Extended Data Fig. 2b, f). The total amount of deformation in each segment also decreases.

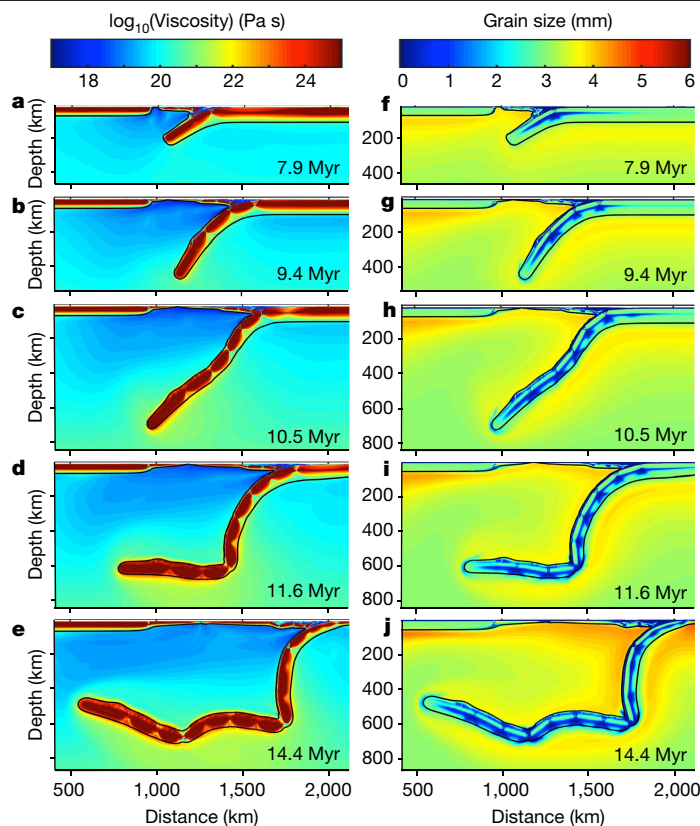


Fig. 1 | Dynamics of subduction and slab segmentation for a 40-million-year-old oceanic plate. A model with 8-km-thick crust formed under present-day mantle temperature conditions (model xbeq, Extended Data Table 2). **a–e**, The evolution of the effective viscosity. **f–j**, The evolution of grain size in the mantle. The solid black lines indicate the position of the 1,225°C isotherm.

Slab segmentation is thus primarily driven by normal fault weakening whereas the ductile damage makes this process more intense, localized and laterally extensive. Ductile creep of mature faults has no influence on segmentation and mainly affects the deformation of segmented slabs in the mantle: weaker (serpentine type) rheology facilitates slab bending and break-off whereas stronger (dry olivine type) rheology produces less deformed slabs (Extended Data Table 2).

The age of the subducting plate also controls the characteristic width of slab segments: older and thus thicker subducting plates show wider slab segments than those of younger plates (compare Extended Data Fig. 3c, g and Extended Data Fig. 3d, h). An increase in the mantle potential temperature, by contrast, promotes slab segmentation and bending by steepening of the slab angles owing to the increased negative slab buoyancy and the reduced amount of viscous resistance of the asthenosphere to slab penetration (compare Fig. 1 and Extended Data Figs. 2a, 4a). This also leads to notable acceleration of subduction and more frequent slab break-off⁶ (compare Fig. 1 and Extended Data Figs. 2a, e, 4a, e).

Many outer-rise fault systems are orientated along pre-existing faulting structures within the oceanic plate^{38,39}. We therefore tested the influence of pre-existing faults by running several models in which these faults have been initially prescribed with different spacing (5 km, 10 km and 20 km) and polarity (towards/outwards the trench) (Extended Data Fig. 5). Similar to the reference model, slab segmentation also developed in the models with pre-existing faults, which have a minor effect on the characteristic segment width (Extended Data Fig. 5). As expected, pre-existing faults are easily reactivated by the plate bending and control the predominant location and polarity of the much deeper outer-rise normal faults (Extended Data Fig. 5).

Weakening of outer-rise faults

Our numerical models suggest that strain weakening of outer-rise normal faults is a key process controlling subducting slab segmentation, and is thus discussed further. Strain weakening of faults is a common assumption of geodynamic models⁴⁰ and is crucial for reproducing a number of strain-localization phenomena in both oceanic and continental lithosphere such as large-offset normal faults⁴⁰, oceanic transform faults⁴¹, and oceanic and continental core complexes⁴². The physics of this process is incompletely understood and may include (but is not limited to) pressurized fluid percolation²⁴, growth of hydrous minerals⁴³, structural softening⁴⁴, shear heating⁴⁵, coseismic weakening and grain-size reduction⁴⁶, and intergranular cavitation⁴⁷. Intense hydration of outer-rise normal faults has been suggested on the basis of seismological, geophysical and theoretical arguments^{2–5,8,31}.

In particular, numerical models⁴ find that the dynamic pressure associated with plate bending may be large enough to overcome the confining lithostatic pressure and cause downwards water suction along outer-rise normal faults. By contrast, analytical models⁹ suggests that such large dynamic pressure cannot be achieved, and lowered seismic velocities within the oceanic lithosphere under the outer rise may instead be explained by thermal cracking. Putting aside such uncertainties regarding the extent of outer-rise fault hydration, it is clear that these structures systematically reveal lowered friction coefficients (≤ 0.3)^{31,48} compared with dry oceanic lithosphere (0.6–0.85)⁴⁹, and only such overall weakening is required for our simplified strain-weakening models (Methods).

Natural evidence for slab segmentation

Our model predicts that, owing to the interplay between the fault weakening and grain-size reduction in the outer rise, subducting slabs are pervasively damaged and can deform easily in a chain-like fashion in the mantle. This new, emergent mechanism provides a self-consistent explanation for the previously proposed subduction dichotomy of strong plates and weak slabs^{10,19–23,30}, which controls the observed slab morphologies^{25,26} in the deep mantle. One of the testable consequences of slab segmentation is the punctuated development of large-offset (throw ≥ 400 m) normal faults located above the localized regions of intense grain-size reduction (Fig. 2a, Extended Data Fig. 6). Mirroring the deep slab morphology, this more localized faulting pattern contrasts with broadly distributed, moderate-offset (throw ≤ 300 m) normal faults as produced by models without grain-size reduction⁴ and/or without intense fault weakening (Fig. 3a, Extended Data Fig. 2b–d, f–h). We predict large-offset normal faults to be transient structures that episodically form close (< 30 km) to the trench and subsequently subduct under the forearc (Extended Data Fig. 6). These structures should thus only be observed at those trenches in nature where the slab-segmentation process is in its mature stage. Fault throw patterns may then vary between different subduction zones and even along the same trench¹ owing to lateral changes in slab-segmentation maturity presumably caused by regional variations in subducting-plate velocity, crustal thickness and cooling age¹. This behaviour is indeed what is observed. Large-offset normal faults are only found very close (< 30 km) to some subduction trenches or under their frontal prisms, such as in the Japan Trench^{6,7,50,51} (Fig. 2c, d) and in the northwest portion of the Middle America Trench^{1,51}, but are absent in other trenches, for example, in most of the Mariana Trench⁵¹ and in the southeast portion of Middle America Trench^{1,51} (Fig. 3c, d). The deepest part of the slab in the bending region in Japan has likewise been inferred to display a localized, intraplate area of reduced effective viscosity based on post-seismic deformation¹⁴. Such deep intraplate weakening is predicted by our model, where this zone corresponds to areas of grain-size reduction that develop in either a strongly localized (mature segment, Fig. 2a) or a more widely distributed (immature segment, Fig. 3a) manner. We analysed (Methods) large-scale fault throw patterns for the models

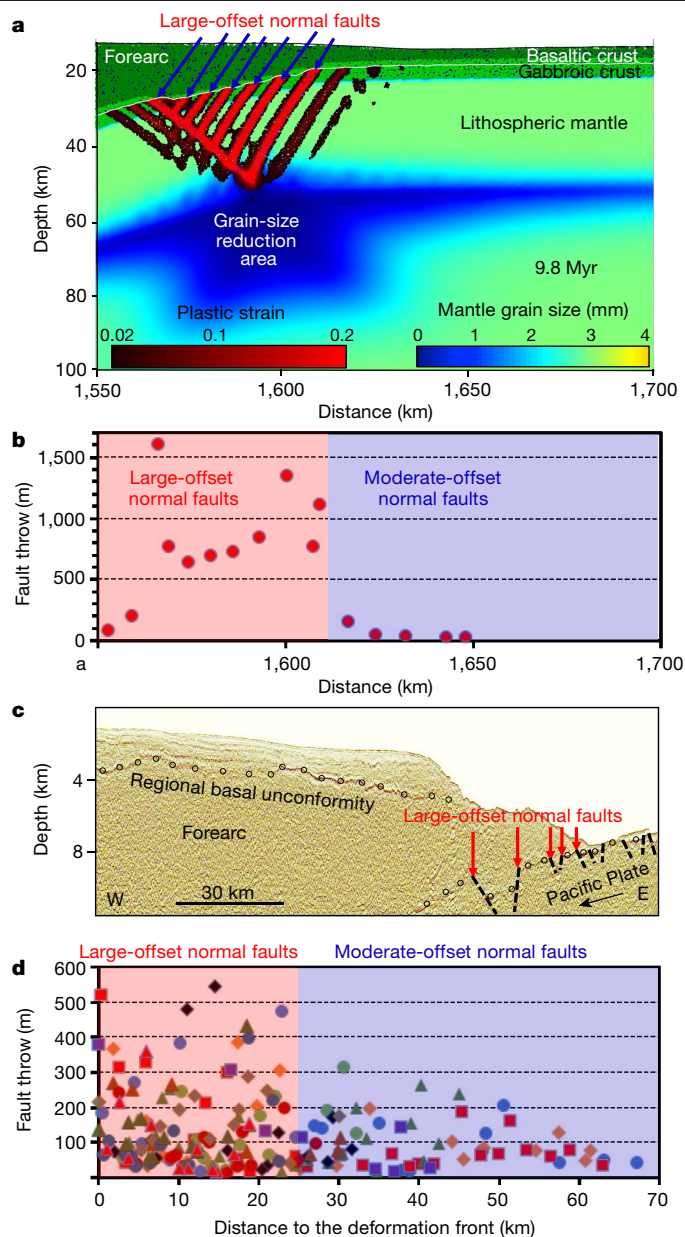


Fig. 2 | Development of large-offset normal faults in the reference model and at the Japan Trench. **a, b**, The modelled normal fault distribution at the stage of mature slab segmentation (model xbeq, Extended Data Table 2, Extended Data Fig. 6). **a**, The distribution of the plastic strain γ (regions with $\gamma > 0.02$ are shown) and mantle grain size in the lithosphere. The solid white line indicates the position of the reference surface along which fault throws are evaluated (Methods). **b**, The numerically modelled fault throw distribution for the profile shown in **a**. Only faults with throw > 20 m are considered. **c**, The seismic profile with the forearc slope morphology, the regional basal unconformity, and subducting Pacific Plate and normal faults indicated⁵⁰. The largest offset is characteristic for the normal fault buried under the frontal prism. **d**, The distribution of fault throws at the Japan Trench measured by ref. ⁷. The data from 13 seismic profiles⁷ across the trench are shown by different symbols. The zones of development of large-offset (throw ≥ 400 m) and moderate-offset (throw ≤ 300 m) normal faults in **b** and **d** are highlighted by pink and blue colours, respectively.

with mature and immature slab segmentation and found significant differences (compare Fig. 2b and Fig. 3b). The model stages of immature slab segmentation show more broadly distributed grain-size reduction and moderate-offset faults with throw that gradually increases towards the trench and then show a plateau at 150–250 m within 40–50 km of

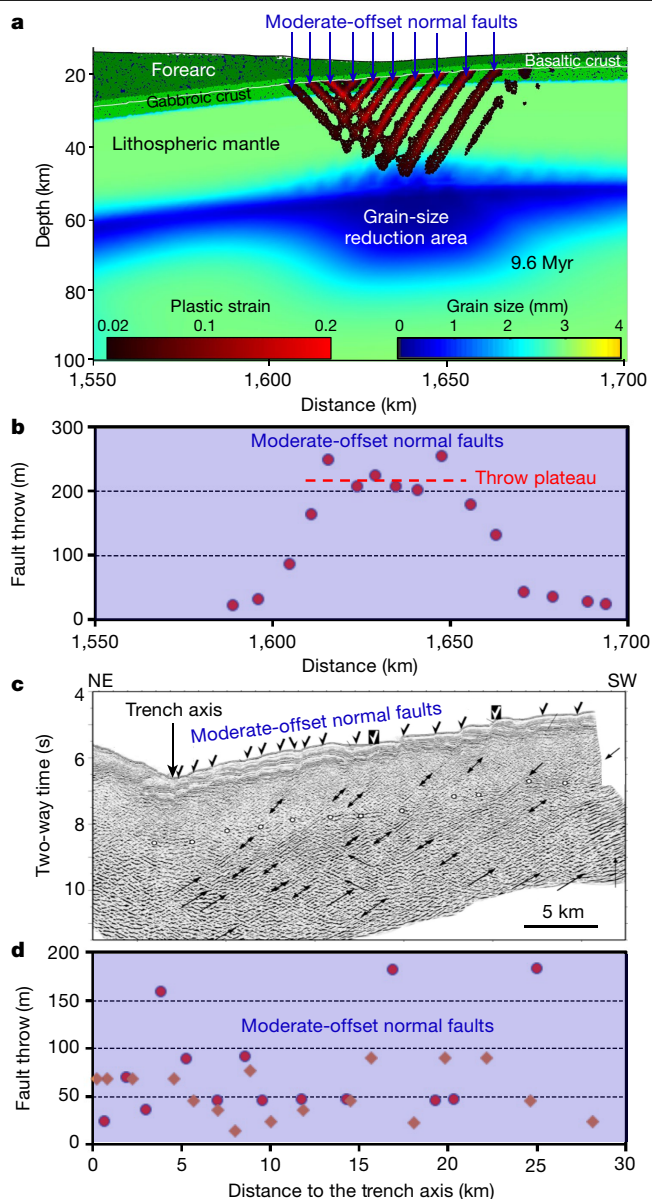


Fig. 3 | Development of moderate-offset (throw ≤ 250 m) normal faults in the reference model and at the southeast portion of the Middle American Trench. **a, b,** The modelled normal fault distribution at the stage of immature slab segmentation (model xbeq, Extended Data Table 2, Extended Data Fig. 6). **a,** The distribution of the plastic strain γ (regions with $\gamma > 0.02$ are shown) and mantle grain size in the lithosphere. The solid white line indicates the position of the reference surface along which fault throws are evaluated (Methods). **b,** The numerically modelled fault throw distribution for the profile shown in **a**. Only faults with throw > 20 m are considered. **c,** The seismic profile with the continental slope morphology, the trench, and subducting Cocos Plate and normal fault positions marked at the surface¹. **d,** The distribution of fault throws at the southeast portion of the Middle American Trench measured by ref.¹. The data from two seismic profiles¹ across the trench are shown.

the trench (Fig. 3b). By contrast, mature slab segmentation shows an abrupt increase and high variability of throws in a narrow zone close to the trench and under the frontal prism (Fig. 2b). These two contrasting cases find their analogy in nature: whereas an abrupt appearance of large-offset normal faults (throw 400–550 m) is documented within the 25-km-wide zone at the Japan Trench (Fig. 2c, d), much more uniformly distributed moderate-offset normal faults (throw < 200 m) are found at the southeast part of the Middle America Trench (Fig. 3c, d). Although slab segmentation may explain the development of the contrasting fault

throw patterns near trenches, the absence of (exposed) large-offset normal faults near some trenches does not imply the absence of slab segmentation as those are transient features (Fig. 2a, c, Extended Data Fig. 6). Broadly variable outer-rise normal faulting patterns worldwide show no correlation with major subduction parameters such as oceanic plate age, subduction velocity and slab pull⁵². Our model provides a self-consistent explanation for this lack of correlation as the spatial distribution and the offsets of outer-rise faults change with time and are mainly dependent on the local maturity of slab segmentation process rather than on the subduction parameters.

Further support for the occurrence of slab segmentation in nature can also be found in high-resolution seismic tomography (Fig. 4, Extended Data Figs. 7, 8). Recent full-waveform imaging yields tomographic models that show unprecedented resolution, such as in the case of Japan¹¹. Both the seismically active part of the slab transiting the upper mantle, and the flat-lying, apparently stalled, part of the slab show segmentation in terms of their seismic velocity. The latter is sensitive to grain size⁵³ and, for Japan, the inferred along-slab positions of the segments' boundaries (Methods) cluster into seven trench-parallel zones of lowered seismic velocity within the slab (Fig. 4d), which bound six individual, 200–425-km-wide segments. The segment width variation along the slab is comparable to our numerical modelling predictions (compare Fig. 4a, b and 4c, d, Extended Data Figs. 3d, h, 4c, g). Compared with our reference model, the wider slab segments inferred for Japan may be due to older seafloor ages (compare Extended Data Fig. 3c, g and Figs. 3d, h, 4c, g). Depth-dependent sensitivity of seismic waves to temperature and imaging imperfections complicate further interpretation, and other explanations for regional slab disruption have been discussed (for example, ref.⁵⁴). However, our grain-size evolution models provide a general explanation that does not rely on a specific convective setting.

Slab segmentation also allows deeper penetration of normal faults into the slab (up to 35–40 km, compare Fig. 2a and Fig. 3a). Global slab seismicity in the outer rise is often characterized by the presence of deep (20–50 km) compressional, thrust-faulting earthquakes. These earthquakes often occur below the elastic core of the subducting plate at temperatures up to 600 °C (ref.³¹), that is, close to the brittle–ductile transition in the mantle lithosphere. The flow-to-friction transition near the base of the seismogenic zone may be characterized by a runaway transition from dislocation and diffusion creep to dilatant deformation, involving incompletely accommodated grain-boundary sliding⁴⁷. Localization of the compressional ductile deformation observed in our numerical experiments (Fig. 2a) and controlled by grain-size reduction may thus create more favourable conditions for deep thrust-faulting; however, is not an ultimate cause for it. The majority of deep compressive earthquakes occur very close (< 30 km) to trenches³¹ where normal faults penetrate deeper into the lithosphere (Figs. 2a, 3a).

Lastly, the formation of a grain-size reduction zone in the bottom part of the slab may contribute to the development of distinct intraslab interfaces that are imaged within both relatively shallow descending slabs¹² (Fig. 5a) and within stagnant slabs in the mantle transition zone¹³ (Fig. 5c). The upper intraslab interface with positive polarity (Fig. 5a, c) is interpreted as the subducted oceanic Moho^{12,13}. By contrast, the lower interface (Fig. 5a, c) is characterized by the large shear-wave velocity reduction and probably requires the presence of melts at the bottom of the lithosphere^{12,13}. This appears consistent with our models as the intense grain-size reduction zone that forms in the bottom of the slab (Fig. 5b, d) should both reduce shear wave velocity⁵³ and decrease permeability, and hence act as a barrier for percolation of melt⁵⁵, thus enabling its accumulation at the bottom of subducted lithosphere.

Occurrence of intermittent subduction

Besides explaining various subduction zone features, brittle–ductile slab segmentation may have further consequences, including for the

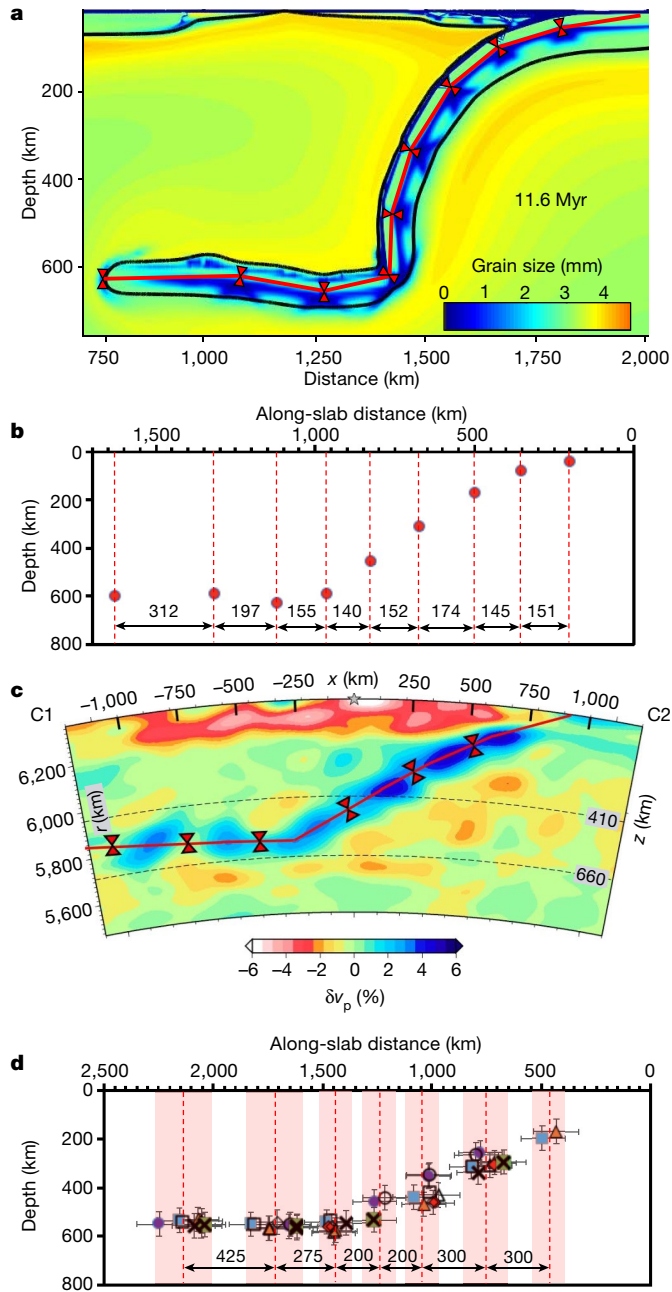


Fig. 4 | Comparison of slab-segment width measured in the reference model and within the Japan slab. **a**, The distribution of segment boundaries (red triangles) defined along the middle-slab line (red solid line) in the numerical model. The solid black line indicates the position of the 1,225 °C isotherm. **b**, The positions of the segment boundaries (dashed red lines) measured along the middle slab line shown in **a**. **c**, The distribution of the v_p velocity anomaly within one of the five analysed along-dip seismic tomography profiles of the Japan slab¹¹ showing clustering of positive anomalies within the slab. The distribution of segment boundaries (red triangles) defined along the middle-slab line (red solid line) is inferred on the basis of visual inspection (Methods). **d**, The positions of segment boundaries (dashed red lines, uncertainty ranges are shown by pink shading) inferred along the five middle slab lines shown in Extended Data Fig. 8. The different symbols correspond to v_p (coloured symbols) and v_s (open symbols) velocity plots for five different profiles: circles, A1–A2; squares, B1–B2; triangles, C1–C2; diamonds, D1–D2; crosses, E1–E2. The black arrows with numbers in **b** and **d** show the along-slab width of the respective segments. Error bars in **d** show uncertainty for defining the positions of segment boundaries in the slab (Methods).

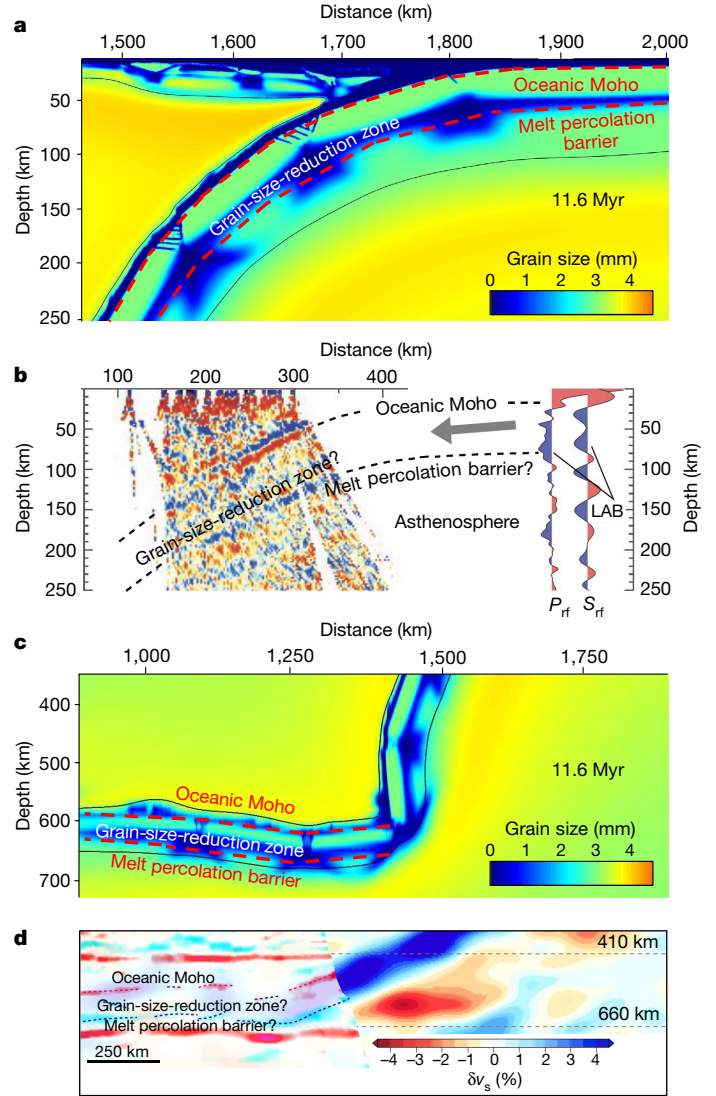


Fig. 5 | Comparison of modelled grain-size distribution in the reference model with seismic discontinuities in the Japan slab. **a**, The formation of the grain-size-reduction zone in the descending slab of the reference model. **b**, P-receiver function image across the Japan Trench (left) and P- and S-receiver functions (P_{rf} , S_{rf}) for the subducting Pacific Plate (right)¹². The red and blue colours indicate velocity increase (from shallow to deep) and decrease at the point, respectively. The upper and lower black dashed lines correspond to the inferred positions of the oceanic Moho and the lithosphere–asthenosphere boundary (LAB), respectively¹². **c**, Subducted grain-size-reduction zone within the stagnant portion of the slab in the mantle transition zone of the reference model. **d**, The slab interfaces (red and blue dashed lines) observed within the stagnant portion of the Japan slab in the mantle transition zone based on a multifrequency receiver function waveform modelling (left)¹³ and seismic tomographic image of the v_s velocity anomaly¹¹ (right). The solid black line in **a** and **c** indicates the position of the 1,225 °C isotherm. The upper and lower dashed red lines in **a** and **c** show the positions of the oceanic Moho and melt percolation barrier, respectively.

stability of the modern style of subduction. In the Archean eon, higher mantle potential temperatures¹⁷ may have significantly reduced both plate strength and mantle resistance to slab penetration, and segmentation may have then induced frequent slab break-off. This could have caused punctuated, episodic (intermittent) subduction^{16,17}. Indeed, our numerical experiments performed even at modestly higher temperatures of 100–150 K compared with the present-day show a strong tendency for slab disruption (Extended Data Fig. 2a, e) and break-off

(Extended Data Fig. 4a, e) in models with grain-size reduction compared with those without (Extended Data Figs. 2b,f, 4b,f). This may imply a sensitive dependence of subduction on mantle temperature, and thus possibly a larger role for an intermittent style of subduction in plate tectonics during our planet's cooling¹⁵ compared with what is expected from mantle convection with memory-free rheologies¹⁷. More generally, our models show that even oceanic lithosphere may be pervasively affected by deformation history, and the associated damage memory affects not only surface deformation at trenches but also how slabs deform and stir their surroundings as they descend into the lower mantle.

Online content

Any methods, additional references, Nature Research reporting summaries, source data, extended data, supplementary information, acknowledgements, peer review information; details of author contributions and competing interests; and statements of data and code availability are available at <https://doi.org/10.1038/s41586-021-03937-x>.

- Ranero, C. R., Phipps Morgan, J. & Reichert, C. Bending-related faulting and mantle serpentinization at the Middle America Trench. *Nature* **425**, 367–373 (2003).
- Ranero, C. R. & Sallarès, V. Geophysical evidence for hydration of the crust and mantle of the Nazca Plate during bending at the North Chile Trench. *Geology* **32**, 549–552 (2004).
- Grevemeyer, I., Ranero, C. R., Flueh, E. R., Kläschen, D. & Bialas, J. Passive and active seismological study of bending-related faulting and mantle serpentinization at the Middle America Trench. *Earth Planet. Sci. Lett.* **258**, 528–542 (2007).
- Faccenda, M., Gerya, T. V. & Burlini, L. Deep slab hydration induced by bending related variations in tectonic pressure. *Nat. Geosci.* **2**, 790–793 (2009).
- Van Avendonk, H. J. A., Holbrook, W. S., Lizarralde, D. & Denyer, P. Structure and serpentinization of the subducting Cocos Plate offshore Nicaragua and Costa Rica. *Geochem. Geophys. Geosyst.* **12**, Q06009 (2011).
- Nakamura, Y., Kodaira, S., Miura, S., Regalla, C., Takahashi, N. High-resolution seismic imaging in the Japan Trench axis area off Miyagi, northeastern Japan. *Geophys. Res. Lett.* **40**, 1713–1718 (2013).
- Boston, B., Moore, G. F., Nakamura, Y. & Kodaira, S. Outer-rise normal fault development and influence on near-trench décollement propagation along the Japan Trench, off Tohoku. *Earth Planets Space* **66**, 135 (2014).
- Shillington, D. J. et al. Link between plate fabric, hydration and subduction zone seismicity in Alaska. *Nat. Geosci.* **8**, 961–964 (2015).
- Korenaga, J. On the extent of mantle hydration caused by plate bending. *Earth Planet. Sci. Lett.* **457**, 1–9 (2017).
- Petersen, R. I., Stegman, D. R. & Tackley, P. J. The subduction dichotomy of strong plates and weak slabs. *Solid Earth*. <https://doi.org/10.5194/se-2016-56> (2016).
- Tao, K., Grand, S. P. & Niu, F. Seismic structure of the upper mantle beneath eastern Asia from full waveform seismic tomography. *Geochem. Geophys. Geosyst.* **19**, 2732–2763 (2018).
- Kawakatsu, H. et al. Seismic evidence for sharp lithosphere–asthenosphere boundaries of oceanic plates. *Science* **324**, 499–502 (2009).
- Wang, X. et al. Distinct slab interfaces imaged within the mantle transition zone. *Nat. Geosci.* **13**, 822–827 (2020).
- Freed, A. M. et al. Resolving depth-dependent subduction zone viscosity and afterslip from postseismic displacements following the 2011 Tohoku-oki, Japan earthquake. *Earth Planet. Sci. Lett.* **459**, 279–290 (2017).
- Herzberg, C. et al. Thermal history of the Earth and its petrological expression. *Earth Planet. Sci. Lett.* **292**, 79–88 (2010).
- van Hunen, J. & van den Berg, A. Plate tectonics on the early Earth: limitations imposed by strength and buoyancy of subducted lithosphere. *Lithos* **103**, 217–235 (2008).
- Sizova, E., Gerya, T., Brown, M. & Perchuk, L. L. Subduction styles in the Precambrian: insight from numerical experiments. *Lithos* **116**, 209–229 (2010).
- Zhong, S. & Davies, G. F. Effects of plate and slab viscosities on the geoid. *Earth Planet. Sci. Lett.* **170**, 487–496 (1999).
- Billen, M. I. & Gurnis, M. Constraints on subducting plate strength within the Kermadec Trench. *J. Geophys. Res.* **110**, B05407 (2005).
- van Summeren, J., Conrad, C. P. & Lithgow-Bertelloni, C. The importance of slab pull and a global asthenosphere to plate motions. *Geochem. Geophys. Geosyst.* **13**, Q0AK03 (2012).
- Garel, F. et al. Interaction of subducted slabs with the mantle transition-zone: a regime diagram from 2-D thermo-mechanical models with a mobile trench and an overriding plate. *Geochem. Geophys. Geosyst.* **15**, 1739–1765 (2014).
- Tao, W. C. & O'Connell, R. J. Deformation of a weak subducted slab and variation of seismicity with depth. *Nature* **361**, 626–628 (1993).
- Wu, B., Conrad, C. P., Heuret, A., Lithgow-Bertelloni, C. & Lallemand, S. Reconciling strong slab pull and weak plate bending: the plate motion constraint on the strength of mantle slabs. *Earth Planet. Sci. Lett.* **272**, 412–421 (2008).
- Gerya, T. V., Connolly, J. A. D. & Yuen, D. A. Why is terrestrial subduction one-sided? *Geology* **36**, 43–46 (2008).
- Čížková, H., van Hunen, J., van den Berg, A. P. & Vlaar, N. J. The influence of rheological weakening and yield stress on the interaction of slabs with the 670-km discontinuity. *Earth Planet. Sci. Lett.* **199**, 447–457 (2002).
- Ribe, N. M. Bending mechanics and mode selection in free subduction: a thin-sheet analysis. *Geophys. J. Int.* **180**, 559–576 (2010).
- Ghosh, A., Becker, T. W. & Zhong, S. J. Effects of lateral viscosity variations on the geoid. *Geophys. Res. Lett.* **37**, L01301 (2010).
- Ranalli, G. *Rheology of the Earth* (Chapman and Hall, 1995).
- Funciello, F. et al. Trench migration, net rotation and slab–mantle coupling. *Earth Planet. Sci. Lett.* **271**, 233–240.
- Liu, L. & Stegman, D. R. Segmentation of the Farallon slab. *Earth Planet. Sci. Lett.* **311**, 1–10 (2011).
- Craig, T. J., Copley, A. & Jackson, J. A reassessment of outer-rise seismicity and its implications for the mechanics of oceanic lithosphere. *Geophys. J. Int.* **197**, 63–89 (2014).
- Bercovici, D., Ricard, Y. Mechanisms for the generation of plate tectonics by two-phase grain-damage and pinning. *Phys. Earth Planet. Inter.* **202–203**, 27–55 (2012).
- Mulyukova, E. & Bercovici, D. Formation of lithospheric shear zones: effect of temperature on two-phase grain damage. *Phys. Earth Planet. Inter.* **270**, 195–212 (2017).
- Mulyukova, E. & Bercovici, D. Collapse of passive margins by lithospheric damage and plunging grain size. *Earth Planet. Sci. Lett.* **484**, 341–352 (2018).
- Mulyukova, E. & Bercovici, D. The generation of plate tectonics from grains to global scales: a brief review. *Tectonics* **38**, 4058–4076 (2019).
- Bercovici, D. & Mulyukova, E. Evolution and demise of passive margins through grain mixing and damage. *Proc. Natl. Acad. Sci. USA* **118**, e201247118 (2021).
- Gurnis, M., Hall, C. & Lavier, L., Evolving force balance during incipient subduction. *Geochem. Geophys. Geosyst.* **5**, Q07001 (2004).
- Masson, D. G. Fault patterns at outer trench walls. *Mar. Geophys. Res.* **13**, 209–225 (1991).
- Ranero, C. R., Villasenor, A., Morgan, J. P. & Weinrebe, W. Relationship between bend-faulting at trenches and intermediate-depth seismicity. *Geochem. Geophys. Geosyst.* **6**, Q12002 (2005).
- Lavier, L. L., Buck, W. R. & Poliakov, A. N. B. Factors controlling normal fault offset in an ideal brittle layer. *J. Geophys. Res.* **105**, 23431–23442 (2000).
- Choi, E., Lavier, L. & Gurnis, M. Thermomechanics of mid-ocean ridge segmentation. *Phys. Earth Planet. Inter.* **171**, 374–386 (2008).
- Whitney, D. L., Teyssier, C., Rey, P. & Buck, W. R. Continental and oceanic core complexes. *Geol. Soc. Am. Bull.* **125**, 273–298 (2013).
- Hirauchi, K., Fukushima, K., Kido, M., Muto, J. & Okamoto, A. Reaction-induced rheological weakening enables oceanic plate subduction. *Nat. Commun.* **7**, 12550 (2016).
- Duretz, T. et al. The importance of structural softening for the evolution and architecture of passive margins. *Sci. Rep.* **6**, 38704 (2016).
- John, T. et al. Generation of intermediate-depth earthquakes by self-localizing thermal runaway. *Nat. Geosci.* **2**, 137–140 (2009).
- Pozzi, G. et al. Coseismic ultramylonites: an investigation of nanoscale viscous flow and fault weakening during seismic slip. *Earth Planet. Sci. Lett.* **516**, 164–175 (2019).
- Verberne, B. A. et al. Microscale cavitation as a mechanism for nucleating earthquakes at the base of the seismogenic zone. *Nat. Commun.* **8**, 1645 (2017).
- Craig, T. J., Copley, A. & Middleton, T. A. Constraining fault friction in oceanic lithosphere using the dip angles. *Earth Planet. Sci. Lett.* **392**, 94–99 (2014).
- Brace, W. F. & Kohlstedt, D. T. Limits on lithospheric stress imposed by laboratory experiments. *J. Geophys. Res.* **85**, 6248–6252 (1980).
- Boston, B., Moore, G. F., Nakamura, Y. & Kodaira, S. Forearc slope deformation above the Japan Trench megathrust: implications for subduction erosion. *Earth Planet. Sci. Lett.* **462**, 26–34 (2017).
- Boneh, Y. et al. Intermediate-depth earthquakes controlled by incoming plate hydration along bending-related faults. *Geophys. Res. Lett.* **46**, 3688–3697 (2019).
- Naliboff, J. B., Billen, M. I., Gerya, T. & Saunders, J. Dynamics of outer rise faulting in oceanic–continental subduction systems. *Geochem. Geophys. Geosyst.* **14**, 2310–2327 (2013).
- Faul, U. H. & Jackson, I. The seismological signature of temperature and grain size variations in the upper mantle. *Earth Planet. Sci. Lett.* **234**, 119–134 (2005).
- Honda, S. Strength of slab inferred from the seismic tomography and geologic history around the Japanese Islands. *Geochem. Geophys. Geosyst.* **15**, 1333–1347 (2014).
- Turner, A. J., Katz, R. F. & Behn, M. D. Grain-size dynamics beneath mid-ocean ridges: Implications for permeability and melt extraction. *Geochem. Geophys. Geosyst.* **16**, 925–946 (2015).

Publisher's note Springer Nature remains neutral with regard to jurisdictional claims in published maps and institutional affiliations.

© The Author(s), under exclusive licence to Springer Nature Limited 2021

Methods

Modelling approach

The thermomechanical two-dimensional numerical code I2VIS is used for the modelling of subduction initiation. It is based on a combination of a finite-difference method, applied on a staggered Eulerian grid, and a marker-in-cell technique^{56,57}. The momentum, mass and energy conservation equations are solved in an Eulerian frame, and physical properties are transported by a Lagrangian. Non-Newtonian, visco-plastic rheologies and variable thermal conductivity are used in the model^{58–63} (Extended Data Table 1), which accounts for major phase transitions in the oceanic crust and mantle as well as adiabatic, radiogenic and frictional internal heating sources. The full details of this method, allowing for its reproduction, are provided elsewhere^{56,57}. Numerical C codes used for the modelling are provided with the paper.

Numerical model design

The initial model setup (Extended Data Fig. 1) corresponds to the one used for spontaneous subduction initiation at an oceanic transform fault^{24,37}. The computational domain is equivalent to $3,000 \times 3,000$ km (Extended Data Fig. 1) and is resolved with an irregular rectangular grid of $1,261 \times 511$ nodes in the horizontal and vertical directions, respectively, and contains 19 million randomly distributed markers. The irregular grid resolution varies from 10×10 km at the model boundaries to 1×1 km in 1,000-km-wide and 200-km-deep subduction zone and outer-rise faulting area. All sides of the model have free-slip mechanical boundary conditions. The free-surface boundary condition atop the crust is implemented by using a 12-km-thick ‘sticky’ air/water layer⁶⁴ with low density (1 kg m^{-3} above 9 km, $1,000 \text{ kg m}^{-3}$ below 9 km) and viscosity (10^{17} Pa s). The initial thermal structure and thickness of the plate (Extended Data Fig. 1) is defined by prescribing a laterally uniform cooling age and respective geotherm⁶⁰ with 273 K at the surface and a mantle potential temperature of 1,523–1,823 K, varied in different experiments (Extended Data Table 2). We explored two types of model setup with different initial conditions. In models with free subducting plate, within 500 km at the right model boundary, the subducting-plate age gradually decreases towards 1,000 yr, which corresponds to a weak mid-ocean ridge located at the boundary (Extended Data Fig. 1a). In models with subducting plate attached to the right model boundary, the subducting-plate age remains unchanged towards the boundary (Extended Data Fig. 1b). An adiabatic gradient of 0.5 K km^{-1} is initially prescribed in the asthenospheric mantle (Extended Data Fig. 1). Within 500 km at the lower boundary, the temperature increases linearly by 744 K to mimic the hot boundary layer at the core–mantle boundary. Temperature-dependent thermal conductivity is used for the mantle and the crust (Extended Data Table 1). The thermal boundary conditions are 273 K at the top, 3,567–3,717 K (depending on the mantle potential temperature) at the bottom and zero heat flux on two other sides of the model. To ensure efficient heat transfer from the surface of the crust, the temperature of the ‘sticky’ air/water is kept constant at 273 K. Gravitational acceleration of 9.81 m s^{-2} has been used in the model.

The surface of the lithosphere evolves by erosion and sedimentation according to the following Eulerian transport equation⁶⁵

$$\frac{\partial z_{\text{es}}}{\partial t} = v_z - v_x \frac{\partial z_{\text{es}}}{\partial x} - v_s + v_e,$$

where x and z are horizontal and vertical coordinates, respectively, z_{es} is the vertical position of the surface as a function of the horizontal distance x , v_z and v_x are the vertical and horizontal components of the material velocity vector at the surface, respectively, and v_s and v_e are the sedimentation and erosion rates, respectively. The sedimentation and erosion rates correspond to the following relations⁶⁶: $v_s = 0 \text{ mm yr}^{-1}$ and $v_e = 0.3 \text{ mm yr}^{-1}$ when $z < 9$ km (the sea-level prescribed in the model), and $v_s = 0.03 \text{ mm yr}^{-1}$ and $v_e = 0 \text{ mm yr}^{-1}$,

when $z > 9$ km. The maximal surface slope for the accumulated sedimentary prism is limited by 17° . Surface processes, however, have a relatively minor role in subduction dynamics and slab morphology in our numerical experiments as follows from test runs without surface processes (Extended Data Table 2).

Density model

We use the extended Boussinesq approximation with the incompressible continuity equation and variable density in the momentum and energy conservation equations. The density of rocks varies with pressure (P) and temperature (T) according to the equation

$$\rho_{P,T} = \rho_0 [1 - \alpha(T - T_0)] [1 + \beta(P - P_0)],$$

where ρ_0 is the standard density at $P_0 = 1 \text{ MPa}$ and $T_0 = 298 \text{ K}$, and $\alpha = 2 \times 10^{-5} \text{ K}^{-1}$ and $\beta = 4.5 \times 10^{-12} \text{ Pa}^{-1}$ are the coefficients of thermal expansion and compressibility, respectively (Extended Data Table 1).

Our models take into account the phase transformations of olivine into wadsleyite and ringwoodite⁶⁷ and into bridgmanite in the mantle⁶⁸. Eclogitization of subducted basaltic and gabbroic crust is taken into account by linearly increasing the density of the crust with pressure from 0% to 16% in the P – T region between the experimentally determined garnet-in and plagioclase-out phase transitions in basalt⁶⁹. Stishovite and perovskite⁶⁸ transitions in the crust are also taken into account for density changes. The physical parameters for each experiment are presented in Extended Data Table 2.

Viscoplastic rheological model

The viscous and brittle (plastic) properties (Extended Data Table 1) are implemented via evaluation of the effective viscosity of the material. For the ductile rheology, the contributions from different flow laws such as dislocation and diffusion creep are taken into account by composite rheology for η_{ductile}

$$\frac{1}{\eta_{\text{ductile}}} = \frac{1}{\eta_{\text{diff}}} + \frac{1}{\eta_{\text{disl}}}, \quad (1)$$

where η_{diff} and η_{disl} are effective viscosities for diffusion and dislocation creep, respectively.

For the crust, constant grain size is assumed and η_{diff} and η_{disl} are computed as

$$\eta_{\text{diff}} = \frac{A}{2\sigma_{\text{cr}}^{n-1}} \exp\left(\frac{E + PV}{RT}\right), \quad (2)$$

$$\eta_{\text{disl}} = \frac{1}{2} A_{\text{disl}}^{1/n} \exp\left(\frac{E + PV}{nRT}\right) \dot{\epsilon}_{\text{II}}^{n-1}, \quad (3)$$

where R is the gas constant, P is pressure, T is temperature (in K), $\dot{\epsilon}_{\text{II}} = \sqrt{1/2(\dot{\epsilon}_{ij})^2}$ is the square root of the second invariant of the strain rate tensor, σ_{cr} is the assumed diffusion–dislocation transition stress, and A , E , V and n are the experimentally determined pre-exponential factor, activation energy, activation volume and stress exponent of the viscous creep, respectively (Extended Data Table 1).

For the mantle, the ductile creep model also takes into account grain-size reduction and growth processes assisted by Zener pinning, and η_{diff} and η_{disl} are calculated according to refs.^{32,33,70–72}. The rheology follows a composite law as in equation (1), wherein

$$\eta_{\text{diff}} = \frac{1}{2} A_{\text{diff}} h^m \exp\left(\frac{E_{\text{diff}} + PV_{\text{diff}}}{RT}\right), \quad (4)$$

$$\eta_{\text{disl}} = \frac{1}{2} A_{\text{disl}}^{1/n} \exp\left(\frac{E_{\text{disl}} + PV_{\text{disl}}}{nRT}\right) \dot{\epsilon}_{\text{II}}^{n-1}, \quad (5)$$

where h is the mean grain size and m is the grain-size exponent. The interplay between diffusion and dislocation creep is controlled by a grain-size-evolution equation dependent on the mechanical work and temperature. The grain-size evolution model relies on several assumptions. (1) The mantle peridotite is assumed to be composed of two well mixed phases: olivine and pyroxene with a fixed volume fraction of 60% and 40%, respectively. These phases are considered to have the same density and rheology. (2) In both phases, the relative motion is considered to be negligible and therefore their velocity is the same. (3) It is assumed that the grain-size distribution is close to a self-similar log-normal distribution. Therefore, it always retains the same shape and its mean variance and amplitude are fully characterized by a unique grain size.

We make the further assumption that the system is in a state known as the pinned-state limit^{32,72} wherein the grain-size evolution is controlled by the pinning of phases by each other (that is, Zener pinning is dominant)³². In these conditions, the grain size is controlled by the roughness r of the interface between the two phases. A relation between the mean grain size h (sufficient to fully describe the system) and the roughness r is given by $h = \frac{r}{\sqrt{h_g}}$, where $h_g \approx \pi/2$ for the phase volume fraction in our model⁷². The roughness evolution is described by the following equations^{32,33,70,73}

$$\frac{dr}{dt} = \frac{\eta G_I}{qr^{(q-1)}} - \frac{f_1 r^2}{\gamma_l \eta} \quad (6)$$

$$G_I = \frac{G_g}{G_{\text{fac}}} \frac{q}{p} r^{(q-p)}, \quad (7)$$

$$G_g = A_g \exp\left(\frac{E_g + PV_g}{RT}\right), \quad (8)$$

$$f_1 = f_0 \exp\left(-2\left(\frac{T}{1,000}\right)^{2.9}\right) \quad (9)$$

where G_I is the interface coarsening, G_g is the grain growth rate, $G_{\text{fac}} = 100$ is the grain growth rate factor, $q = 4$ is the roughness coarsening exponent, $p = 2$ is the grain-size coarsening exponent, γ_l is the surface tension, $A_g = 2 \times 10^{(4-6p)}$ is the pre-exponential factor, $E_g = 3 \times 10^5$ is the grain-growth activation energy, $V_g = V_{\text{diff}}$ is the grain-growth activation volume, f_1 is the fraction of mechanical work Ψ converted to interface damage resulting in grain-size reduction; $f_0 = 0.001$ is the interface damage at 1,000 K, and $\eta = 3\varphi_{\text{ol}}\varphi_{\text{px}}$ is interface area density depending on the volume fractions of olivine ($\varphi_{\text{ol}} = 0.6$) and pyroxene ($\varphi_{\text{px}} = 0.4$) in the mantle.

The ductile rheology is combined with a brittle (plastic) rheology to yield an effective viscous-plastic rheology using the following upper limit for the ductile viscosity

$$\eta_{\text{ductile}} \leq \frac{C + \mu P}{2\dot{\epsilon}_{\text{II}}}, \quad (10)$$

$$\mu = \mu_0 - \gamma\mu_y \text{ for } \gamma \leq \gamma_0 \text{ and } \mu = \mu_1 \text{ for } \gamma > \gamma_0,$$

$$\gamma = \int \sqrt{\frac{1}{2}(\dot{\epsilon}_{ij}^{\text{(plastic)}})^2} dt,$$

where μ is the internal friction coefficient, (μ_0 and μ_1 are the initial and final internal friction coefficient, respectively, Extended Data Table 1), $\mu_y = (\mu_0 - \mu_1)/\gamma_0$ is the rate of faults weakening with integrated plastic strain γ (γ_0 is the upper strain limit for the fracture-related weakening), C is the rock compressive strength at $P = 0$ (Extended Data Table 1), t is

time and $\dot{\epsilon}_{ij}^{\text{(plastic)}}$ is the plastic strain rate tensor. It is also assumed that the mantle inside outer-rise normal faults that reached the upper strain limit (γ_0) is serpentinized and has the respective rheology (Extended Data Table 1).

Computing fault throw from numerical models

Fault throw was evaluated on the basis of integrated plastic strain γ stored on markers. To have a conservative estimate of the plastic strain related to normal faulting, we first defined a reference surface (white solid line in Figs. 2a, 3a) located inside the rheologically strong gabbroic layer at 3.5-km vertical distance above the oceanic Moho. Then, strain on markers found within 250-m vertical distance around this reference surface has been averaged at the nearest vertical grid lines intercepting the reference surface. Faults were then identified as the local maxima of the plastic strain γ , for which an affective fault throw magnitude M was estimated as

$$M = \gamma D \sin(\alpha), \quad (11)$$

where $D = 1$ km is a characteristic fault width in our models (as faults always localize within one grid cell) and $\alpha = 56^\circ$ is the characteristic normal fault dip angle in the models. We used a throw of 20 m as the sensitivity threshold for this numerical approach. The Matlab code throw.m used for this calculation is provided with the paper.

Defining of slab-segment width from seismic tomography

We analysed five regularly spaced along-dip seismic tomography profiles of the Japan slab¹¹ (Extended Data Fig. 4) for both v_p (pressure wave) and v_s (shear wave) velocity variations (Extended Data Fig. 5). First, we inferred middle-slab lines along each profile that were drawn along the most intense positive seismic velocity anomalies within the slab. Then we identified segments boundaries along the middle slab lines, separately for v_p and v_s velocity, by assuming that they correspond to zones of clear intraslab seismic velocity decrease located in between individual positive seismic velocity anomalies. Segment boundary depths and along-slab positions were then defined at their locations within the middle-slab line and plotted on the same plot for different profiles and seismic velocities (Fig. 5d). By doing that we assumed that, owing to the variable quality of seismic data, not all segment boundaries can be always visible in each profile (Extended Data Fig. 8) whereas they should statistically cluster into similar positions measured along the slab (Fig. 5d). Error bars for this visual inspection correspond to around ± 50 km for the depth of the middle-slab line and around ± 100 km for defining thesegment boundary position along the line (Fig. 5d).

Data availability

All input files used in the numerical modelling are available at <https://doi.org/10.17605/OSF.IO/bnvth>. Source data are provided with this paper.

Code availability

The C and Matlab codes used for numerical experiments and visualization are available at <https://doi.org/10.17605/OSF.IO/bnvth>.

56. Gerya, T. V. & Yuen, D. A., Characteristics-based marker-in-cell method with conservative finite-differences schemes for modeling geological flows with strongly variable transport properties. *Phys. Earth Planet. Inter.* **140**, 293–318 (2003).
57. Gerya, T. V. *Introduction to Numerical Geodynamic Modelling* 2nd edn (Cambridge Univ. Press, 2019).
58. Karato, S. & Wu, P. Rheology of the upper mantle: a synthesis. *Science* **260**, 771–778 (1993).
59. Hofmeister, A. M. Mantle values of thermal conductivity and the geotherm from phonon lifetimes. *Science* **283**, 1699–1706 (1999).
60. Turcotte, D. L. & Schubert, G. *Geodynamics* (Cambridge Univ. Press, 2002).
61. Clauser, C. & Huenges, E. in *Rock Physics and Phase Relations* AGU Reference Shelf 3 (ed. Ahrens, T. J.) 105–126 (American Geophysical Union, 1995).
62. Hirth, G. & Kohlstedt, D. in *Subduction Factor Monograph* Vol. **138** (ed. Eiler, J.) 83–105 (American Geophysical Union, 2003).

63. Hilaret, N. B. et al. High-pressure creep of serpentine, interseismic deformation, and initiation of subduction. *Science* **318**, 1910–1913 (2007).
64. Schmeling, H. et al. A benchmark comparison of spontaneous subduction models: Towards a free surface. *Phys. Earth Planet. Inter.* **171**, 198–223 (2008).
65. Gerya, T. V. & Yuen, D. A. Rayleigh–Taylor instabilities from hydration and melting propel “cold plumes” at subduction zones. *Earth Planet. Sci. Lett.* **212**, 47–62 (2003).
66. Baitsch-Ghirardello, B., Gerya, T. V. & Burg, J.-P. Geodynamic regimes of intra-oceanic subduction: implications for arc extension vs. shortening processes. *Gondwana Res.* **25**, 546–560 (2014).
67. Katsura, T. & Ito, E. The system Mg_2SiO_4 – Fe_2SiO_4 at high pressures and temperatures: precise determination of stabilities of olivine, modified spinel, and spinel. *J. Geophys. Res.* **94**, 663–670 (1989).
68. Ito, E. et al. Negative pressure–temperature slopes for reactions forming $MgSiO_3$ perovskite from calorimetry. *Science* **219**, 1275–1278 (1990).
69. Ito, K. & Kennedy, G. C. in *The Structure and Physical Properties of the Earth's Crust* Geophysical Monograph Series 14 (ed. Heacock, J. G.) 303–314 (American Geophysical Union, 1971).
70. Bercovici, D. & Ricard, Y. Generation of plate tectonics with two-phase grain-damage and pinning: source–sink model and toroidal flow. *Earth Planet. Sci. Lett.* **365**, 275–288 (2013).
71. Bercovici, D. & Ricard, Y. Plate tectonics, damage and inheritance. *Nature* **508**, 513–516 (2014).
72. Bercovici, D., Schubert, G. & Ricard, Y. Abrupt tectonics and rapid slab detachment with grain damage. *Proc. Natl Acad. Sci. USA* **112**, 1287–1291 (2015).
73. Rozel, A., Ricard, Y. & Bercovici, D. A thermodynamically self-consistent damage equation for grain size evolution during dynamic recrystallization. *Geophys. J. Int.* **184**, 719–728 (2011).
74. Hayes, P. et al. Slab2, a comprehensive subduction zone geometry model. *Science* **362**, 58–61 (2018).
75. Bird, P. An updated digital model of plate boundaries. *Geochem. Geophys. Geosyst.* **4**, 1027 (2003).

Acknowledgements This work was supported by SNF projects 200021_182069 and 200021_192296 and ETH+ project BECCY (to T.V.G.) and NSF EAR-1853856 (to T.W.B.) and NSF EAR-1853184 (to D.B.). The simulations were performed on the ETH-Zurich Euler and Leonhard clusters.

Author contributions T.V.G. programmed the numerical code, designed the study and conducted the numerical experiments; D.B. formulated the grain size evolution algorithm and programmed the numerical code; and T.W.B. compiled and annotated Extended Data Figs. 7, 8 and provided related text. All authors discussed the results, problems and methods, and contributed to interpretation of the data and writing the paper.

Competing interests The authors declare no competing interests.

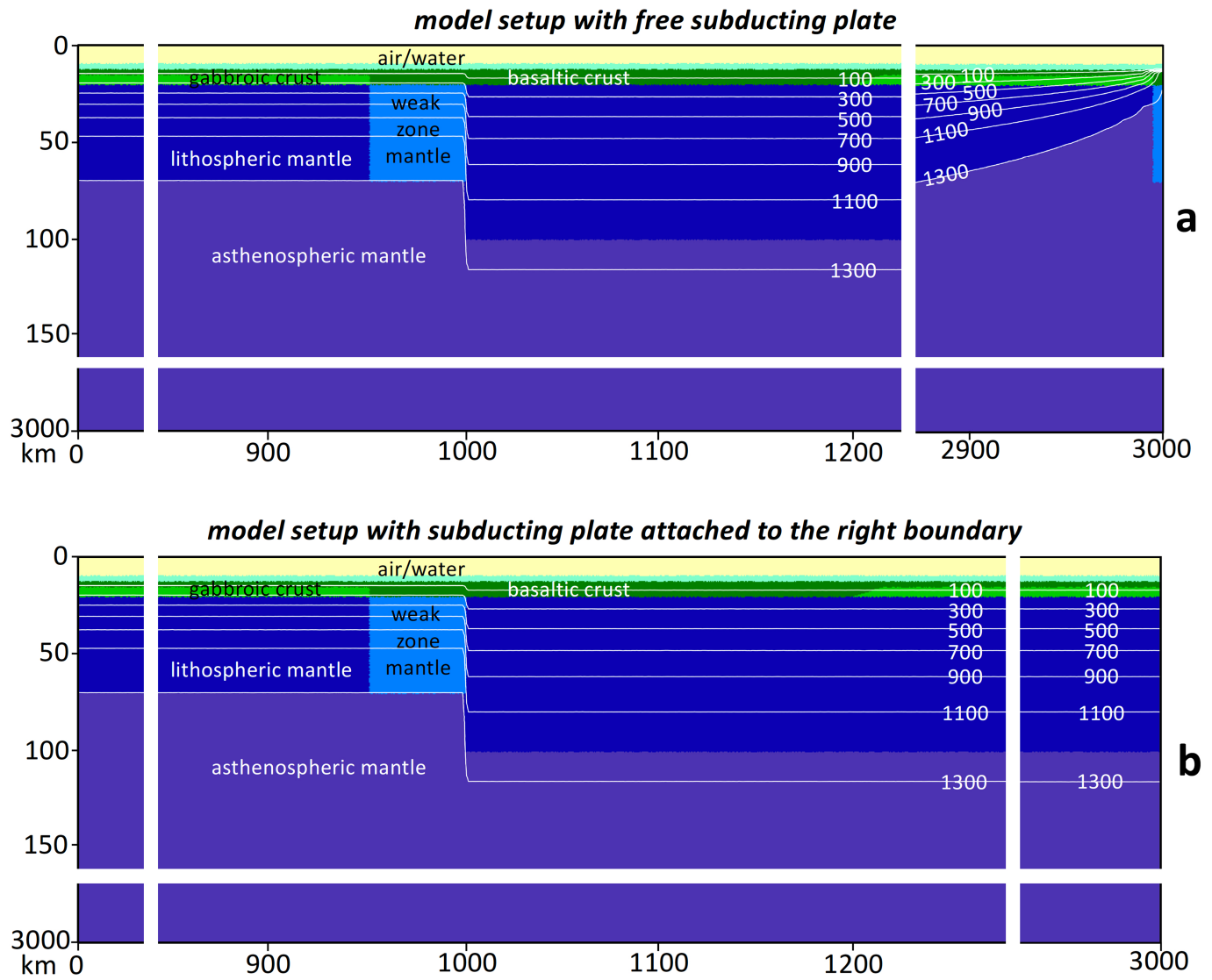
Additional information

Supplementary information The online version contains supplementary material available at <https://doi.org/10.1038/s41586-021-03937-x>.

Correspondence and requests for materials should be addressed to T. V. Gerya.

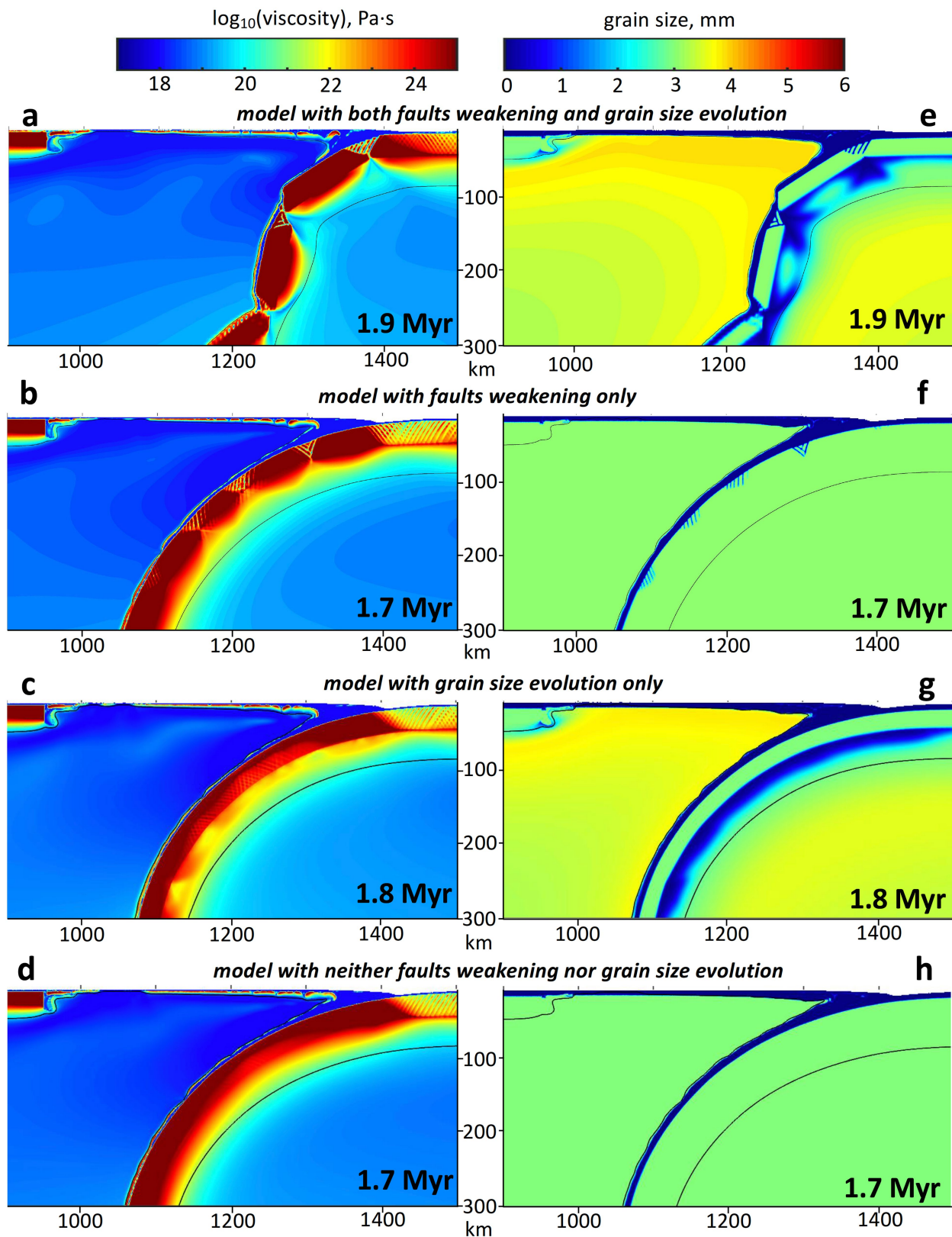
Peer review information *Nature* thanks the anonymous reviewers for their contribution to the peer review of this work. Peer reviewer reports are available.

Reprints and permissions information is available at <http://www.nature.com/reprints>.



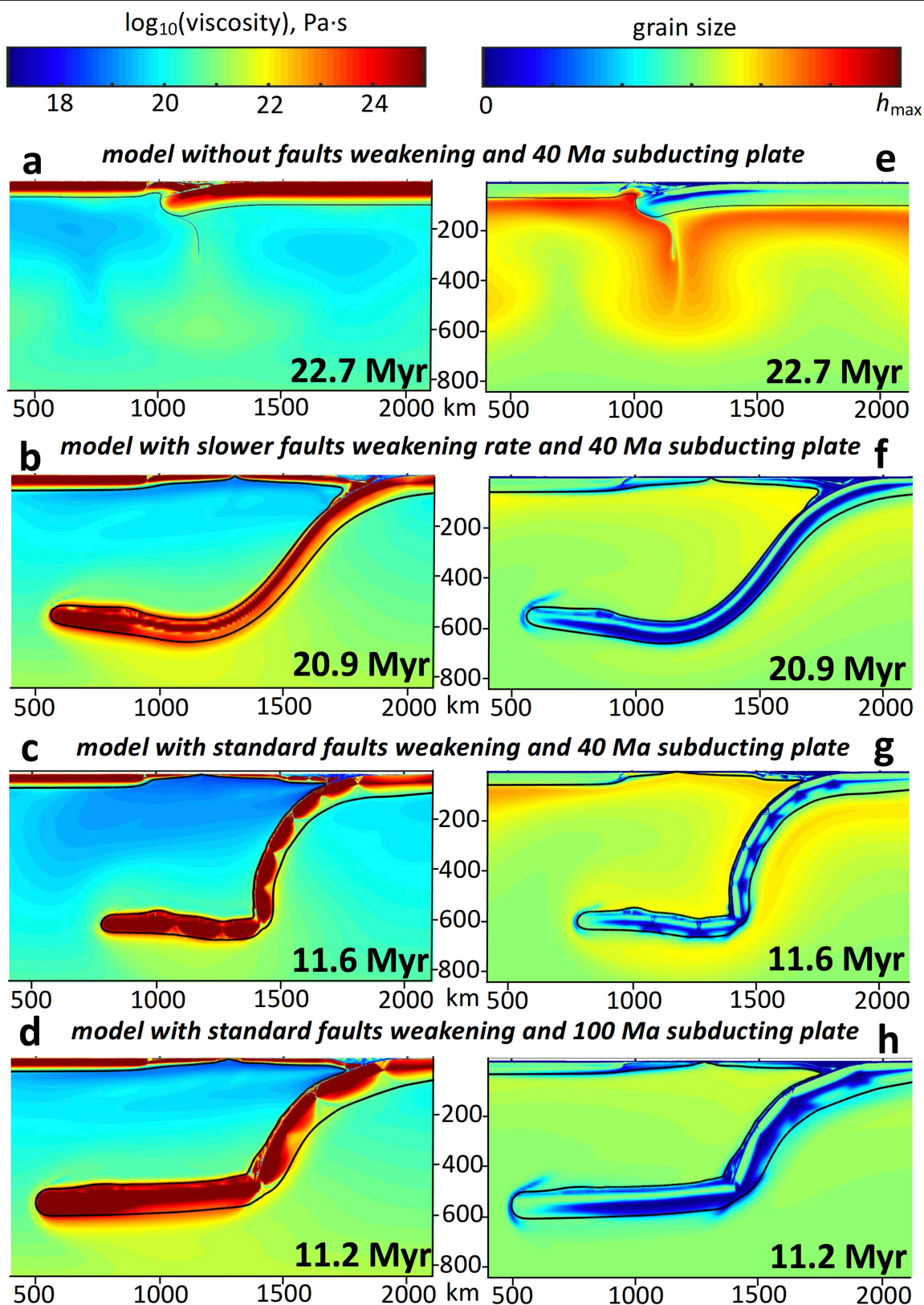
Extended Data Fig. 1 | Initial conditions for two types of subduction model explored in this study. a. Model setup with free subducting plate detached from the right model boundary; subducting plate age changes to 1,000 yr linearly with the distance within 500 km at the right model boundary. **b.** Model

setup with subducting plate attached to the right model boundary; subducting plate age does not change toward the boundary. White lines with numbers are isotherms in °C.



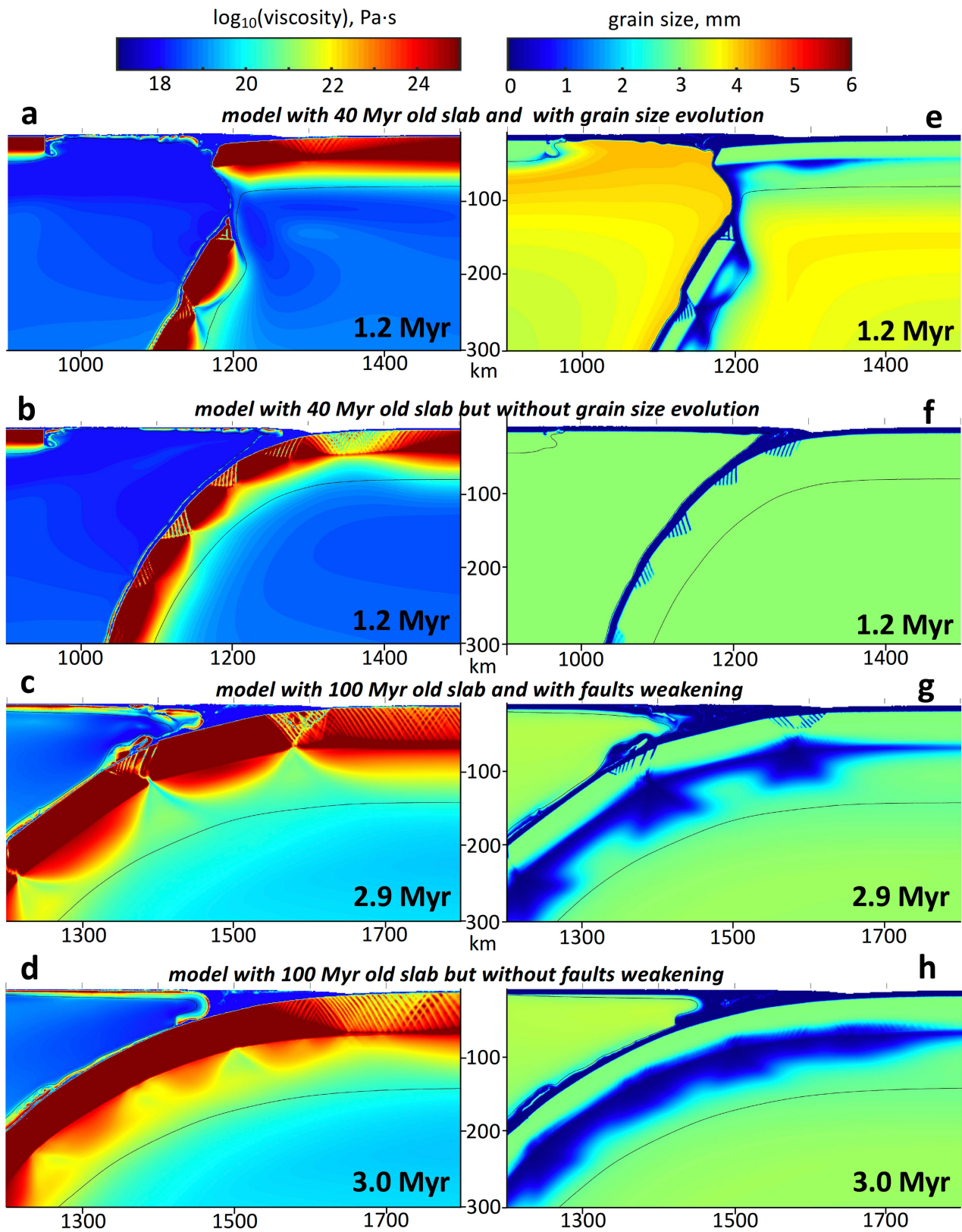
Extended Data Fig. 2 | Influence of faults weakening and grain size evolution on subduction dynamics. The distribution of the effective viscosity (left column, panels a–d) and grain size in the mantle (right column, panels e–h). **a, e**, Model with both faults weakening and grain size evolution (model xbeqc, Extended Data Table 2). **b, f**, Model with faults weakening but without grain size evolution (model xbeqca, Extended Data Table 2). **c, g**, Model with grain size evolution but without faults weakening ($\mu_0 = \mu_1 = 0.6$ for the

lower oceanic crust and lithosphere-asthenosphere mantle, model xbeqcb, Extended Data Table 2). **d, h**, Model with neither fault weakening nor grain size evolution ($\mu_0 = \mu_1 = 0.6$ for the lower oceanic crust and lithosphere-asthenosphere mantle, model xbeqcc, Extended Data Table 2). Mantle temperature is taken 100 K higher than present day values. Other parameters are the same as in the reference model (Fig. 1). Solid black lines indicate position of 1225°C isotherm.



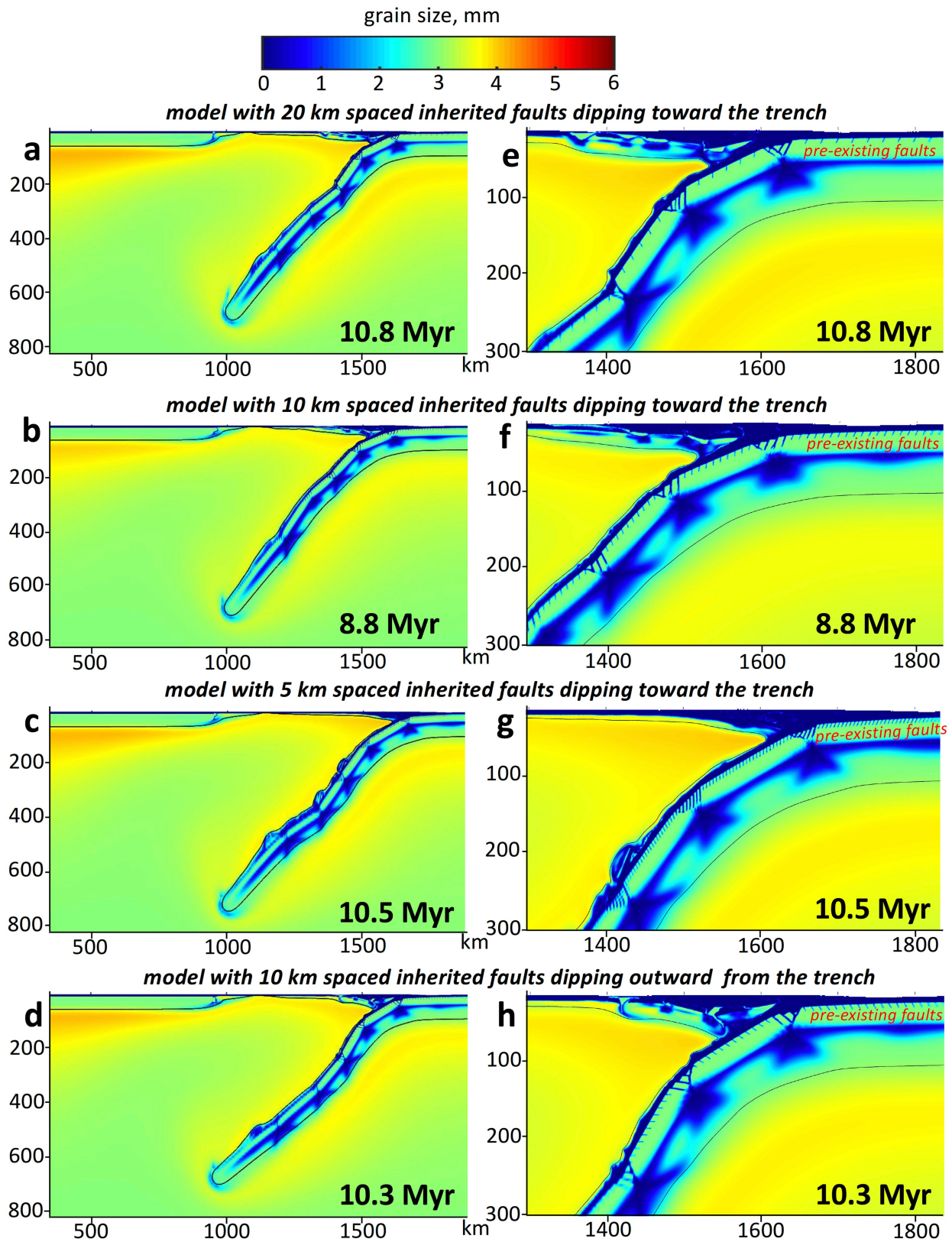
Extended Data Fig. 3 | Influence of model parameters on subduction dynamics in models with standard grain size evolution. The distribution of the effective viscosity (left column, panels a–d) and grain size in the mantle (right column, panels e–h). **a, e**, Failed subduction initiation in the model with 40 Ma subducting plate but without faults weakening ($\mu_0 = \mu_1 = 0.6$ for the lower oceanic crust and lithosphere-asthenosphere mantle, $h_{\text{max}} = 6$ mm for the grain size color code, model xbeqab, Extended Data Table 2). **b, f**, No slab segmentation in the model with 40 Myr old slab but with 2.5 times slower rate of faults

weakening with strain ($h_{\text{max}} = 10$ mm, model xbes, Extended Data Table 2). **c, g**, Reference slab segmentation model with 40 Myr subducting plate and standard faults weakening ($h_{\text{max}} = 6$ mm, model xbeq, Fig. 1, Extended Data Table 2). **d, h**, Wider slab segments in the model with 100 Myr old slab and standard fault weakening ($h_{\text{max}} = 10$ mm, model xber, Extended Data Table 2). Mantle temperature is taken at present day values. Other parameters are the same as in the reference model (Fig. 1). Solid black lines indicate position of 1225°C isotherm.



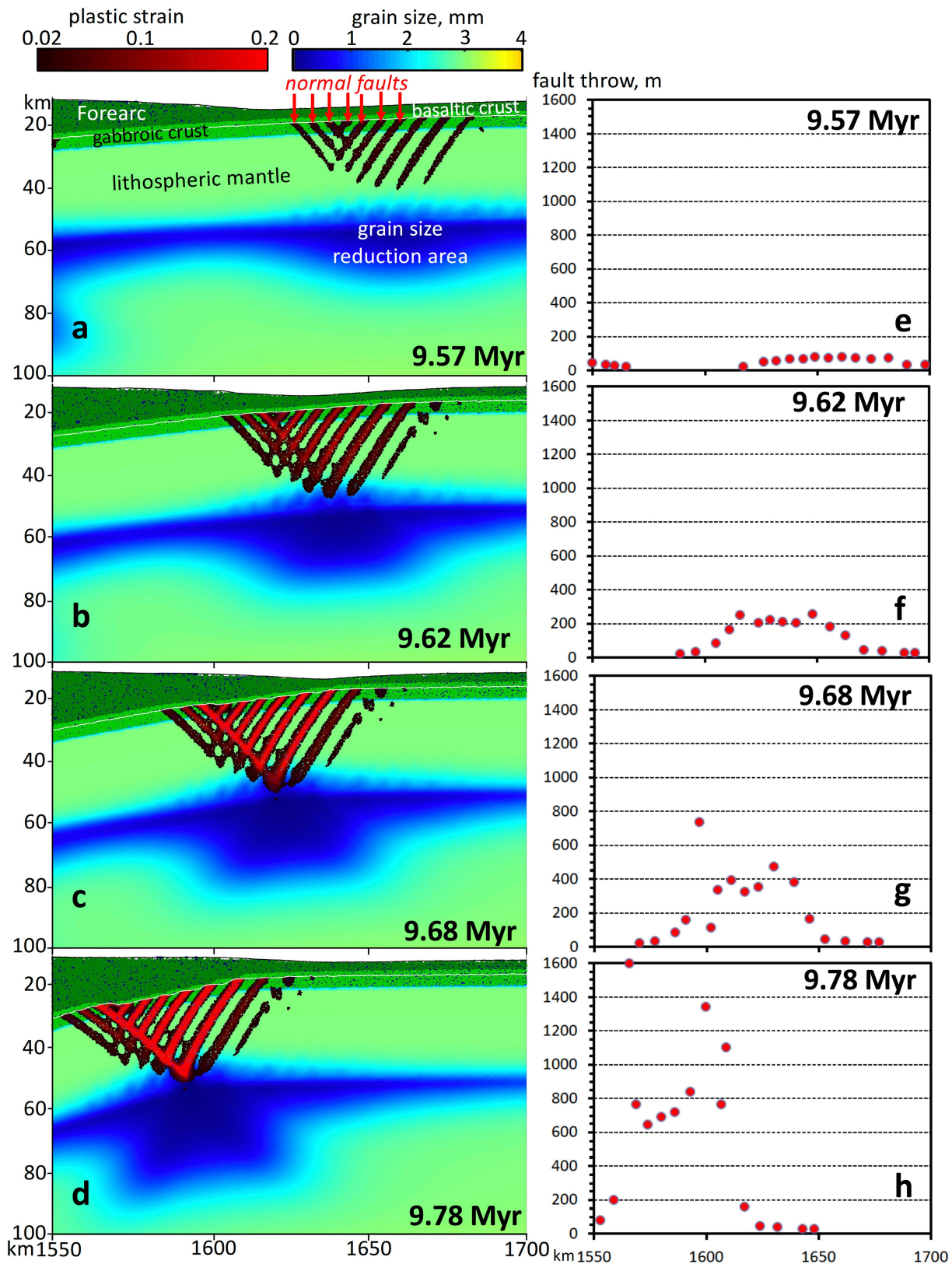
Extended Data Fig. 4 | Influence of grain size evolution and faults weakening on subduction dynamics. The distribution of the effective viscosity (left column, panels a–d) and grain size in the mantle (right column, panels e–h). **a, e**, Model with both fault weakening and grain size evolution (40 Myr old slab, model xbeqd, Extended Data Table 2). **b, f**, Model with fault weakening but without grain size evolution (40 Myr old slab, model xbeqda,

Extended Data Table 2). **c, g**, Model with both fault weakening and grain size evolution (100 Myr old slab, model xbeqq, Extended Data Table 2). **d, h**, Model with grain size evolution but without fault weakening (100 Myr old slab, model xbeqs, Extended Data Table 2). Mantle potential temperature in **a, b, e, f** is 150 K higher than present day values. Other parameters are the same as in the reference model (Fig. 1). Solid black lines indicate position of 1225 °C isotherm.



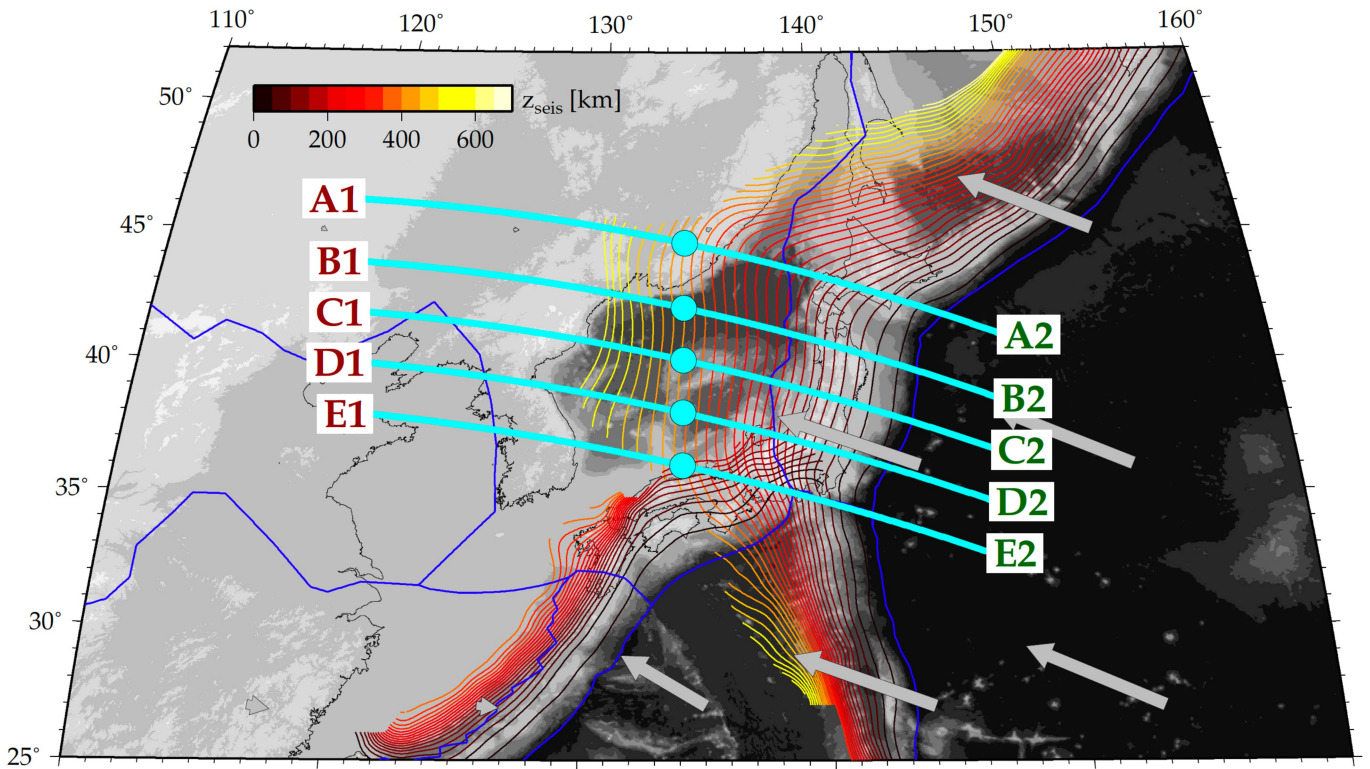
Extended Data Fig. 5 | Influence of pre-existing faults in the subducting plate on slab segmentation and subduction dynamics. a, e, Model with 20 km spaced faults dipping toward the trench (model xbeql, Extended Data Table 2). **b, f,** Model with 10 km spaced faults dipping toward the trench (model xbeqm, Extended Data Table 2). **c, g,** Model with 5 km spaced faults dipping toward the trench (model xbeqn, Extended Data Table 2). **d, h,** Model

with 10 km spaced faults dipping outward the trench (model xbeqo, Extended Data Table 2). Pre-existing faults are prescribed as 1 km wide and 14 km deep zones of weak basaltic crust and serpentinized mantle within stronger gabbroic crust and lithospheric mantle, respectively (Extended Data Table 1). Initial fault dip is 63°.

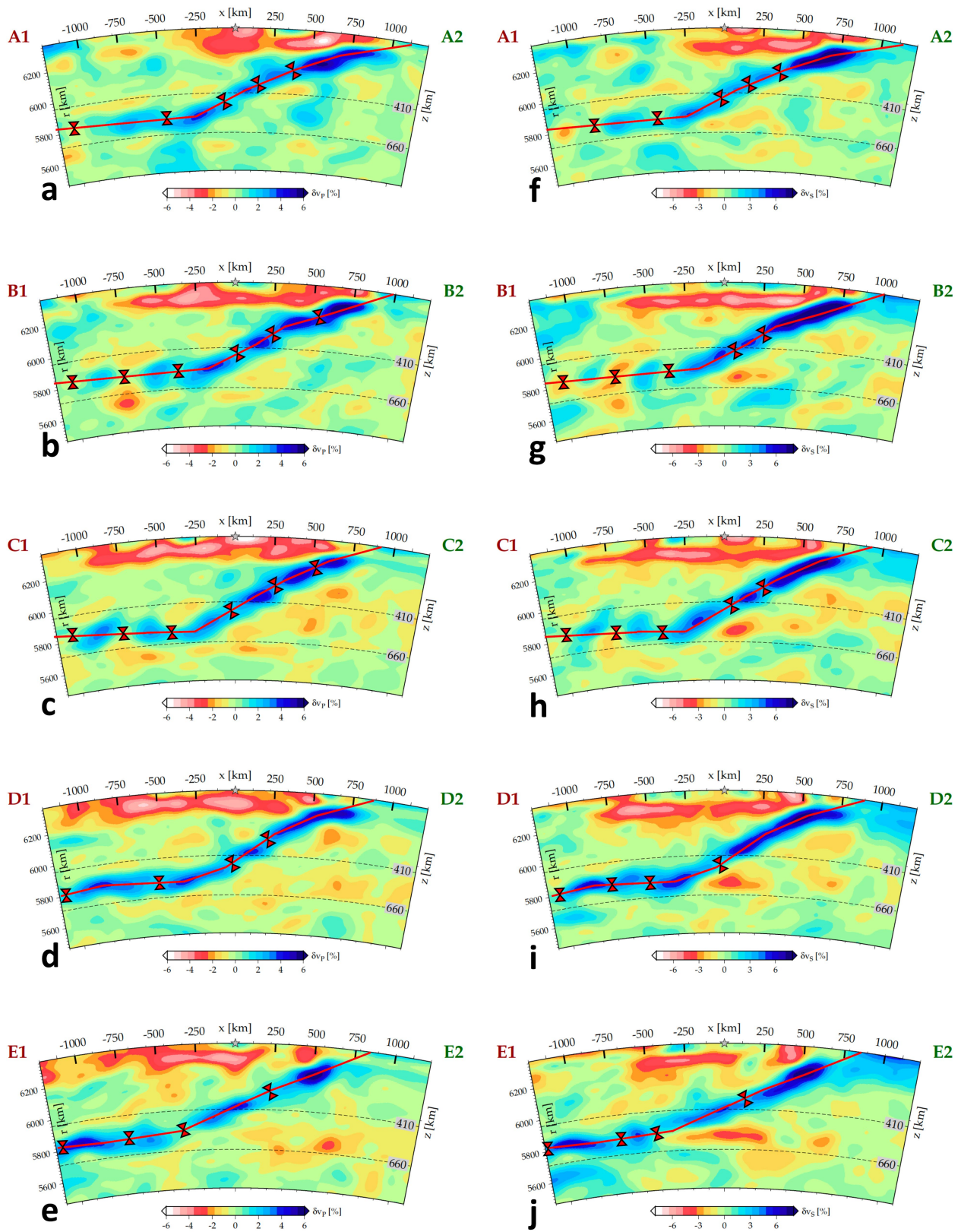


Extended Data Fig. 6 | Gradual development of large-offset normal faults in the reference model (Fig. 1). a–d, Distribution of the plastic strain γ (regions with $\gamma > 0.02$ are shown) and mantle grain size in the lithosphere.

Solid white line indicates position of the reference surface along which fault throws are evaluated (Methods). e–h, Fault throw distribution for respective time steps shown in a–d. Only faults with throw > 20 m are considered.



Extended Data Fig. 7 | Positions of five along-dip seismic tomography profiles (blue solid lines with circles) for the Japan slab analysed in Fig. 4c, d and **Extended Data Fig. 8**. Colour code corresponds to slab upper surface based on seismicity depths from SLAB2.0 model⁷⁴. Solid blue lines show positions of plate boundaries⁷⁵.



Extended Data Fig. 8 | Tomographic images for five analyzed (Fig. 4d, Methods) seismic tomography profiles of the Japan slab (Extended Data Fig. 7). The distribution of v_p (left column, panels a–e) and v_s (right column, panels f–j) seismic velocity anomaly is based on the tomography model of

Tao et al.¹³. Positions of segment boundaries (red triangles) defined along the middle-slab line (red solid lines) are inferred on the basis of visual inspection (Methods).

Extended Data Table 1 | Physical properties of rocks⁵⁸⁻⁶³ used in numerical experiments

Material	ρ_0 , (kg/m ³)	Thermal conductivity, (W/m/K at T_K, P_{MPa})	Flow law
Upper oceanic crust (basalt)	3000	$1.18+474/(T+77) \times \exp(0.00004P)$	wet quartzite, $A = 1.97 \times 10^{17} \text{ Pa}^n \text{ s}$, $n=2.3$, $E=154000 \text{ J/mol}$, $V=8 \text{ J/mol/MPa}$, $\sigma_{cr}=3 \times 10^4 \text{ Pa}$, $C=0.3 \text{ MPa}$, $\mu_0=0$, $\mu_1=0$
Lower oceanic crust (gabbro)	3000	$1.18+474/(T+77) \times \exp(0.00004P)$	plagioclase An ₇₅ , $A = 4.80 \times 10^{22} \text{ Pa}^n \text{ s}$, $n=3.2$, $E=238000 \text{ J/mol}$, $V=8 \text{ J/mol/MPa}$, $\sigma_{cr}=3 \times 10^4 \text{ Pa}$, $C=0.3 \text{ MPa}$, $\mu_0=0.6$, $\mu_1=0.2$
Lithosphere - asthenosphere mantle	3300	$0.73+1293/(T+77) \times \exp(0.00004P)$	dry olivine, $m=3$, $A_{diff} = 6.67 \times 10^{14} \text{ Pa s}$, $E_{diff}=375000 \text{ J/mol}$, $V_{diff}=5 \text{ J/mol/MPa}$, $A_{disl} = 9.09 \times 10^{15} \text{ Pa}^n \text{ s}$, $n=3.5$, $E_{disl}=530000 \text{ J/mol}$, $V_{disl}=23 \text{ J/mol/MPa}$, $C=0.3 \text{ MPa}$, $\mu_0=0.6$, $\mu_1=0.2$
Weak zone mantle	3250	$0.73+1293/(T+77) \times \exp(0.00004P)$	wet olivine, $h=0.001 \text{ m}$, $m=2.5$, $A_{diff}=2.7 \times 10^{18} \text{ Pa s}$, $E_{diff}=240000 \text{ J/mol}$, $V_{diff}=4 \text{ J/mol/MPa}$, $A_{disl} = 2.56 \times 10^{14} \text{ Pa}^n \text{ s}$, $n=3.0$, $E_{disl}=430000 \text{ J/mol}$, $V_{disl}=10 \text{ J/mol/MPa}$, $C=0.3 \text{ MPa}$, $\mu_0=0$, $\mu_1=0$
Serpentinized mantle inside normal faults	3200	$0.73+1293/(T+77) \times \exp(0.00004P)$	serpentine, $A = 3.21 \times 10^{36} \text{ Pa}^n \text{ s}$, $n=3.8$, $E=8900 \text{ J/mol}$, $V=3.2 \text{ J/mol/MPa}$, $\sigma_{cr}=3 \times 10^6 \text{ Pa}$, $C=0.3 \text{ MPa}$, $\mu_0=0.2$, $\mu_1=0.2$

Extended Data Table 2 | Conditions and results of numerical experiments

Model	Mantle potential temp. (K)	Subduct. plate age (Myr)	Free subduct. plate (yes/no)	Surface processes (yes/no)	Faults weakening (yes/no)	Grain size evolution (yes/no)	γ_0	Results, Figures
xbeq	1573	40	yes	yes	yes	yes	0.2	sustained subduction, slab segmentation, Figs. 1, 2a,b, 3a,b, 4a,b, 5a,c, Extended Data Figs. 3c,g, 6
xbeqaa	1573	40	yes	yes	yes	no	0.2	failed subduction initiation
xbeqab ^c	1573	40	yes	yes	no ^e	yes	n/a	failed subduction initiation, Extended Data Fig. 3a,c
xbeqac ^c	1573	40	yes	yes	no ^e	no	n/a	failed subduction initiation
xbeqad	1573	40	yes	no	yes	yes	0.2	sustained subduction, slab segmentation
xbeqab	1623	40	yes	yes	yes	yes	0.2	sustained subduction, slab segmentation
xbeqba	1623	40	yes	yes	yes	no	0.2	sustained subduction, no slab segmentation
xbeqc	1673	40	yes	yes	yes	yes	0.2	sustained subduction, slab segmentation and breakoff, Extended Data Fig. 2a,e
xbeqca	1673	40	yes	yes	yes	no	0.2	sustained subduction, weak slab segmentation, Extended Data Fig. 2b,f
xbeqcb ^e	1673	40	yes	yes	no ^e	yes	n/a	sustained subduction, no slab segmentation, Extended Data Fig. 2c,g
xbeqcc ^e	1673	40	yes	yes	no ^e	no	n/a	sustained subduction, no slab segmentation, Extended Data Fig. 2d,h
xbeqcd	1673	40	yes	no	yes	yes	0.2	sustained subduction, no strong slab segmentation
xbeqce ^a	1673	40	yes	yes	yes	yes	0.2	sustained subduction, slab segmentation
xbeqcf ^b	1673	40	yes	yes	yes	yes	0.2	sustained subduction, slab segmentation and breakoff
xbeqcg ^c	1673	40	yes	yes	yes	yes	0.2	sustained subduction, slab segmentation
xbeqd	1723	40	yes	yes	yes	yes	0.2	sustained subduction, strong slab segmentation and breakoff, Extended Data Fig. 4a,c
xbeqda	1723	40	yes	yes	yes	no	0.2	sustained subduction, no slab segmentation, Extended Data Fig. 4b,f
xbeqe	1773	40	yes	yes	yes	yes	0.2	failed subduction initiation
xbeqea	1773	40	yes	yes	yes	no	0.2	failed subduction initiation
xbeqf	1823	40	yes	yes	yes	yes	0.2	failed subduction initiation
xbeqfa	1823	40	yes	yes	yes	no	0.2	failed subduction initiation
xbeqg	1523	40	yes	yes	yes	yes	0.2	failed subduction initiation
xbeqga	1523	40	yes	yes	yes	no	0.2	failed subduction initiation
xbeqh	1748	40	yes	yes	yes	yes	0.2	slab segmentation, subduction arrested after slab breakoff
xbeqi	1773	40	no	yes	yes	yes	0.2	sustained subduction, strong slab segmentation and breakoffs
xbeqia	1773	40	no	yes	yes	no	0.2	sustained subduction, slab segmentation and breakoff
xbeqj	1823	40	no	yes	yes	yes	0.2	sustained subduction, strong slab segmentation and breakoffs
xbeqja	1823	40	no	yes	yes	no	0.2	sustained subduction, slab segmentation and breakoff
xbeqk	1573	40	no	yes	yes	yes	0.2	slab segmentation, subduction arrested after slab breakoff
xbeqka	1573	40	no	yes	yes	no	0.2	failed subduction initiation
xbeql ^f	1573	40	yes	yes	yes	yes	0.2	sustained subduction, slab segmentation, Extended Data Fig. 5a,c
xbeqm ^g	1573	40	yes	yes	yes	yes	0.2	sustained subduction, slab segmentation, Extended Data Fig. 5b,f
xbeqn ^h	1573	40	yes	yes	yes	yes	0.2	sustained subduction, slab segmentation, Extended Data Fig. 5c,g
xbeqo ⁱ	1573	40	yes	yes	yes	yes	0.2	sustained subduction, slab segmentation, Extended Data Fig. 5d,h
xbeqp ⁱ	1573	100	yes	yes	yes	yes	0.2	sustained subduction, slab segmentation
xbeqq	1573	100	yes	yes	yes	yes	0.2	sustained subduction, slab segmentation, Extended Data Fig. 4c,g
xbeqr ⁱ	1573	100	yes	yes	no	yes	0.2	sustained subduction, weak slab segmentation
xbeqs	1573	100	yes	yes	no	yes	0.2	sustained subduction, weak slab segmentation, Extended Data Fig. 4d,h
xbeqt ⁱⁱ	1573	40	yes	yes	yes	yes	0.2	failed subduction initiation
xbequ ^l	1573	40	yes	yes	yes	yes	0.2	failed subduction initiation
xbeqv ⁱⁱ	1573	40	no	yes	yes	yes	0.2	failed subduction initiation
xbeqw ^l	1573	40	no	yes	yes	yes	0.2	failed subduction initiation
xber ^d	1573	100	yes	yes	yes	yes	0.2	sustained subduction, slab segmentation, Extended Data Fig. 3d,h
xbes ^d	1573	40	yes	yes	yes	yes	0.5	sustained subduction, no slab segmentation, Extended Data Fig. 3b,f

^a dry olivine rheology⁶² ($h=3$ mm) of mature faults with $\gamma > \gamma_0$.

^b serpentine rheology⁶³ ($\sigma_{cr}=3 \times 10^4$ Pa) of mature faults with $\gamma > \gamma_0$.

^c dry olivine rheology⁶² ($h=0.03$ mm) of mature faults with $\gamma > \gamma_0$.

^d $h=5$ mm initial grain size.

^e no faults weakening, $\mu_0=\mu_1=0.6$ for the lower oceanic crust and lithosphere - asthenosphere mantle.

^f pre-existing 20 km spaced faults dipping toward the trench in the subducting plate.

^g pre-existing 10 km spaced faults dipping toward the trench in the subducting plate.

^h pre-existing 5 km spaced faults dipping toward the trench in the subducting plate.

ⁱ pre-existing 10 km spaced faults dipping outward the trench in the subducting plate.

^l free overriding plate detached from the left model boundary (similarly to free subducting plate, Extended Data Fig. 1a).